2015-08-01

Jet and Droplet Impingement on Superhydrophobic Surfaces

Jonathan Glenn Stoddard
Brigham Young University

Jet and Droplet Impingement on Superhydrophobic Surfaces

Jonathan Glenn Stoddard

A thesis submitted to the faculty of
Brigham Young University
in partial fulfillment of the requirements for the degree of

Master of Science

Julie Crockett, Chair
R. Daniel Maynes
Steven E. Gorrell

Department of Mechanical Engineering

Brigham Young University

August 2015

ABSTRACT

Jet and Droplet Impingement on Superhydrophobic Surfaces

Jonathan Glenn Stoddard
Department of Mechanical Engineering, BYU
Master of Science

The effect of superhydrophobicity on liquid water impingement on a flat horizontal surface was explored. The surfaces combined a hydrophobic surface chemistry with a patterned microstucture in order to produce high contact angles with water. Three sets of experiments were performed, one for jet impingement and two for droplet impingement, which advance previous work in characterizing the interaction of water and superhydrophobic surfaces.

Jet impingement experiments were performed to characterize a transitional regime between an unsubmerged and a completely submerged superhydrophobic surface by varying an imposed downstream depth. For low downstream depths, the surface remained unsubmerged and displayed only break up of the thin film, while at high downstream depths, the surface was completely submerged and only a hydraulic jump occurred. Within the transition, the surface was partially submerged and both thin film breakup and a hydraulic jump were observed. Experiments were performed for three Reynolds numbers, Re, ranging from 1.9×10^4 to 2.2×10^4 (based on the volume flow rate). For all Re, the transition was characterized by a reduction in the hydraulic jump radius as downstream depth increased. Also, as Re increased, the downstream depths over which the transition occurred was greater.

When a droplet impinges on a surface covered with a liquid film, a thin liquid wall, or crown, forms and propagates outward. Here a comparison of this crown dynamic was made for smooth hydrophilic surfaces and superhydrophobic (SH) surfaces patterned with post or rib microfeatures. Due to the high contact angle of the SH surfaces, a relatively thick film ($h \approx 5$ mm) of water was required to maintain a film. This resulted in negligible differences between the surfaces utilized. Droplet train impingement on the same post and rib SH surfaces was also investigated. When each individual droplet impinged on the surface, a crown formed which spread out radially until reaching a semi-stable or regularly oscillating breakup diameter. At this point, the water would either build up or breakup into droplets or filaments and then continue radially outward. In some cases the crown would break up, causing splashing. A comparison to previous experiments on hydrophilic surfaces shows a distinct difference in splashing at low frequency. The breakup diameter was measured over a Weber number range of 72-2800. The data was collapsed as a function of a combination of the Reynolds number (Re), Capillary number (Ca), and Strouhal number (St), resulting in $Re^{0.7}CaSt$. The rib SH surface displayed an elongated breakup due to the anisotropic surface features. The breakup diameter for the droplet train was compared to the breakup diameter which has been shown to occur with a jet impinging on a SH surface.

Keywords: superhydrophobic surfaces, jet impingement, droplet impingement, droplet train

ACKNOWLEDGMENTS

I would like to express my appreciation first and foremost to Dr. Crockett, Dr. Maynes,Dr. Gorrell, and Dr. Iverson for their assistance throughout my graduate career. Also, I could not have completed my research without the help of Evan Bee who helped to collect and analyze data. I would like to thank Joseph Prince, Cristian Clavijo, Richard Perkins, Ken Forster, Kevin Cole, and all other Brigham Young University students and faculty who have assisted in developing my setup and learning the necessary tools to perform this research. I also thank my wife, Kimberly, and other family members who gave me the strength and support I needed to complete this work.

This research was supported by the National Science Foundation (Grant CBET-1066356).

TABLE OF CONTENTS

LIST OF TABLES

LIST OF FIGURES

NOMENCLATURE

Ca	Capillary number, $V\mu/\sigma$
D	Crown diameter
F_H	Hydrostatic force
F_m	Force due to momentum, $\int \rho V dA$
F_S	Surface tension force
H	Crown height
Q	Volumetric flow rate
R_a	Averaged surface roughness
R_B	Radius of breakup
R_F	Radius of free hydraulic jump
R_H	Radius of hydraulic jump
Re	Reynolds number
St	Strouhal number, fd/V
V	Impingement velocity
We	Weber number, $\rho V^2 d/\sigma$
a	Jet radius
d	Droplet diameter
d_B	Breakup diameter
d_j	Jet diameter
f	Droplet frequency
h	Downstream depth
θ	Contact angle
θ_a	Advancing contact angle
θ_r	Receding contact angle
θ_s	Static contact angle
λ	Viscosity length, $(\nu/f)^{1/2}\sigma/(\rho\nu)$
μ	Dynamic viscosity
ν	Kinematic viscosity
ρ	Density
σ	Surface tension
τ	Nondimensional time Vt/d

CHAPTER 1. INTRODUCTION

1.1 Motivation

Fluid dynamics involving superhydrophobic (SH) surfaces has been of great interest in recent research. This is due to the manner in which these surfaces alter the fluid flow compared to smooth hydrophilic and even hydrophobic surfaces. Initially, SH surfaces were observed in plants and insects. The lotus leaf, for example, utilizes wax coated papillae to cause water from rain or dew to build up and roll off. As droplets roll off, they remove particulates to keep the leaf fully exposed to sunlight. High contact angles, due to reduced liquid adhesion to the surface, result in interfaces with surfaces tension acting opposite from a hydrophilic surface. Such high contact angles promote quick droplet removal from these surfaces resulting in self-cleaning properties. The surface tension at these interfaces promotes liquid breakup in instances of jet and droplet train impingement. In the case of a liquid jet impinging a SH surface, the spreading thin film formed by the impingement breaks up into droplets instead of forming a hydraulic jump as it would on a hydrophilic surface. This, however, has been shown to occur only when hydrostatic forces are also reduced, which will otherwise revert to having a hydraulic jump.

Another characteristic of SH surfaces is an apparent slip which occurs due to the liquid sitting above air filled cavities with reduced shear. When the scale of flow nears that of the microfeatures, as does the thin film in jet or droplet impingement, the effect of this slip becomes appreciable. By using patterned surface features, such as microribs, the effect of the slip can be utilized to decrease skin friction and, in the case of anisotropic surface features, partially redirect the flow.

Both jet and droplet impingement are common in heat transfer operations, but primarily utilize hydrophilic surfaces. However, SH surfaces have properties which would be beneficial, such as self-cleaning and liquid removal. Recent research has focused on describing the unique hydrodynamic properties involved in jet and droplet impingement on SH surfaces, including jet

impingement on submerged and unsubmerged SH surfaces and single droplet impingement on dry SH surfaces. This research seeks to increase understanding by exploring a transition regime in which a jet impinges on a partially submerged SH surface. Similarly, the dynamics of droplet impingement on a liquid coated SH surface and droplet train impingement on a SH surface are explored.

1.2 Background

1.2.1 Superhydrophobicity

SH surfaces are characterized by their high contact angle, $\theta > 120°$, as shown in Figure 1.1, and are a result of hydrophobic surface chemistry combined with a micro or nano surface structure. The high contact angle is due to the reduced adhesion of the liquid to the surface. This allows the surface tension of the liquid to pull the liquid into a sphere in order to reduce the thermodynamic energy [2]. The lotus leaf is often referred to as a prime example of a SH surface, where the leaves use hydrophobic waxes covering a micro-topography of papillae [3]. There are various approaches to duplicate this phenomenon. Etching silicon or growing carbon nanotubes are common methods developed to generate a microstructure [4]. These methods can be utilized to create random or carefully patterned microstructures such as posts or ribs as shown in Figure 1.2. Other methods, such as using abrasives or a spray-on coating, will only allow for randomized microstructures. Natively hydrophilic surfaces (surfaces with $\theta < 90°$) are often coated with a hydrophobic coating such as wax or Teflon®. An important characteristic of these surfaces is the cavity fraction, $F_c =$

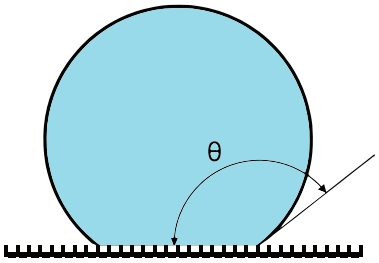

Figure 1.1: Drawing of a droplet of water sitting on a SH surface. The contact angle, θ, is the angle from the surface in contact with the water to the liquid surface extending outward.

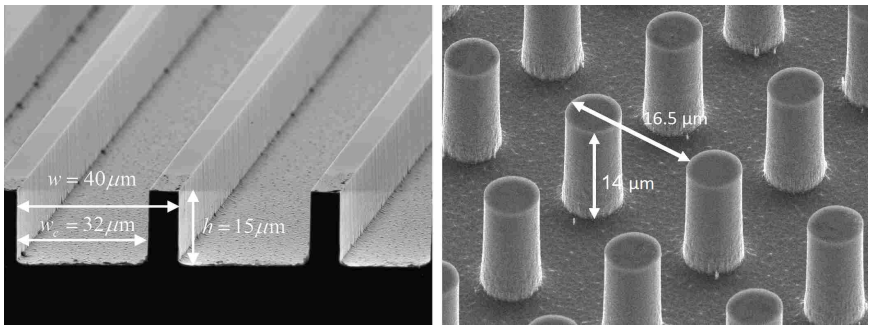

Figure 1.2: SEM images of microscale rib (left) and post (right) surface topographies as designed and created with common photolithography techniques on silicon wafers.

$A_c/(A_c+A_s)$, defined as the ratio of the cavity area, A_c, and the total projected area of the cavity and microfeatures, A_c+A_s. For the rib surface in Figure 1.2 the cavity fraction is $F_c = w_c/w$ where w_c is the width of the cavity and w is the width of a rib and cavity.

There are two states which exist with SH surfaces, Cassie-Baxter and Wenzel, as shown in Figure 1.3. In the first the liquid remains above the cavities of the microstructure in what is termed the Cassie-Baxter state. The meniscus between structures is maintained by the surface tension. If the pressure exceeds the Laplace pressure, defined as $\Delta P = \sigma(1/R_1 + 1/R_2)$, where σ is the surface tension and R_1 and R_2 are the radii of curvature of the meniscus, then the fluid penetrates the cavities. When the surface wets in this fashion, it is termed the Wenzel state and the surface has a reduced contact angle [5]. The apparent contact angle, ϕ^*, is shown in Equation 1.1 as a function

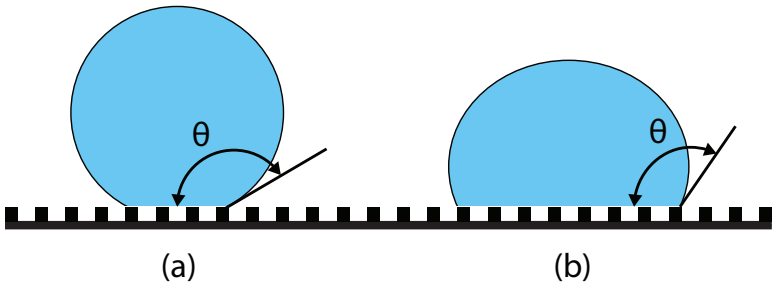

Figure 1.3: Drawing of a droplet of water sitting on a SH surface in the (a) the Cassie-Baxter state with the liquid sitting above the mircrostructure and (b) Wenzel state with the liquid penetrating the microstructure.

of cavity fraction, F_c, the initial contact angle, ϕ, and the roughness ratio of the wetted area over the projected area, r_w [6].

$$cos(\phi^*) = r_w(1 - F_c)cos(\phi) - f_c \tag{1.1}$$

For ϕ larger than 90°, ϕ^* increases as F_c increases.

Because of the liquid-air interface in the cavities of the microstructure, if a uniform liquid is flowing above the surface the shear at these cavities is negligible and the total shear at the surface decreases. This decrease is characterized by an apparent slip at the surface as shown in Figure 1.4 [7–9]. The slip can be expressed by the slip length, which is the projected length into the surface where the velocity would reach the no-slip condition. The magnitude of slip increases for increasing F_c and w [10]. Slip at the surface reduces friction drag, which is desirable in microchannels and microfluidic devices where viscous effects from the wall require large pressure gradients to drive the flow [11].

In addition to drag reducing mechanisms, research has displayed self-cleaning attributes in which liquid droplets roll off SH surfaces while removing particulates [12]. This property makes SH surfaces useful in heat transfer applications where self-cleaning reduces fouling, which in turn increases the consistency of heat transfer [13]. In condensers, condensation buildup is decreased by allowing water to roll or even jump off surfaces [14]. Recent research has also demonstrated potential anti-icing properties of SH surfaces due to water droplets leaving the surface before freezing and by reducing nucleation [15].

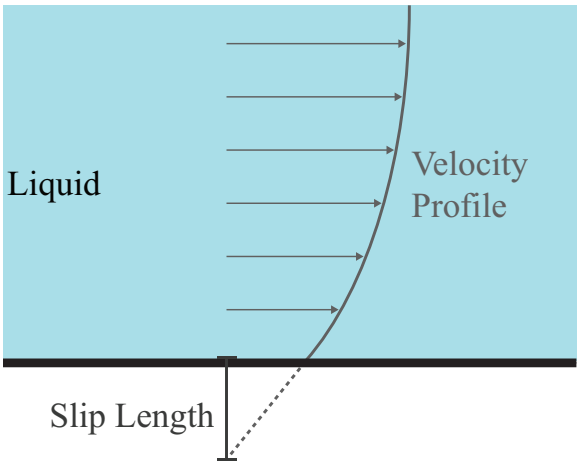

Figure 1.4: Schematic of a liquid flowing over a surface displaying a partial slip velocity.

Since this work focuses on the effect of superhydrophobicity on jet and droplet impingement, a background of these areas of research are given next.

1.2.2 Jet Impingement

When a jet impinges on a surface, it spreads out into a thin film as shown in Figure 1.5. The thin film radial velocity decreases as it moves outward due to viscous drag and radial spreading. The fluid momentum for a thin slice of the spreading film is defined as $M = \int \rho V^2 dA$, where ρ is the density, V is the velocity profile across the thickness of the film, and A is the cross-sectional area (spanning the circumferential length and film thickness). Once the velocity decreases sufficiently, M will reach a balance with the hydrostatic force, F_H, of a resulting or imposed downstream depth [16]. At this radius, R_H, a hydraulic jump is created where the surface height of the liquid becomes that of the downstream depth, h. Surface tension, F_S, can also play a role, acting radially inward from the hydraulic jump. Bush and Aristoff showed that surface tension will decrease the hydraulic jump radius, but the effect is diminished as the jump radius increases [17]. Prince et al. modeled slip on the surface in the thin film region and found the presence of slip resulted in increased momentum, which increased the jump radius. This effect was more pronounced for greater jump radii as slip had greater area over which to exert influence [18]. The model used by Prince et al. [19] has been compared to jet impingement on SH surfaces patterned with microribs [20]. The model showed good agreement to the data with a maximum deviation of 8% in the direction of the ribs and 10-16% in the direction transverse to the ribs. The error in the transverse

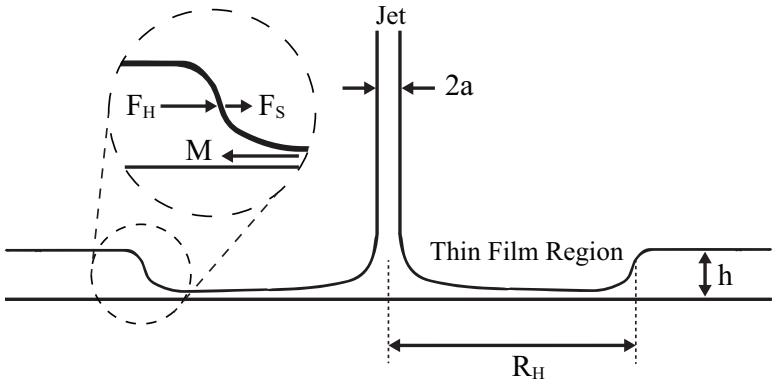

Figure 1.5: Diagram showing a side view of hydraulic jump formation due to a laminar jet impinging on a surface. The dominant forces are shown at the location of the hydraulic jump.

direction was attributed to utilizing an inaccurate value of slip in the transverse direction, but was not explored further. Johnson [20] and Prince et al. [19] found that altering the pattern on the surface (e.g., ribs or posts) can change the resulting shape of the hydraulic jump due to the difference in slip in each direction. Both also showed that as the downstream depth was increased or Weber number, $We = \rho V^2 d/\sigma$, decreased, the hydraulic jump diameter decreased due to an increase in the hydrostatic force compared to the fluid momentum.

It has been demonstrated that without an imposed downstream depth, jet impingement on a hydrophobic or SH surface can result in breakup of the thin film instead of a hydraulic jump [20, 21]. Figure 1.6 shows jet impingement and thin film breakup on a SH surface. In this case, the high contact angle results in a significant surface tension force pulling inward. This causes the thin film on the surface to break up into droplets due to surface tension forces at a critical location denoted as the breakup radius, R_B. At this point, the force due to momentum, M, balances with the surface tension, F_S. Johnson [20] and Maynes et al. [21] demonstrated that at a Weber number of about 1000, breakup of the thin film into droplets began occurring. At this condition there is enough momentum to generate droplets that continue to move outward. Otherwise, the fluid flows outward as filaments or simply builds up on the surface. Droplet coalescence and periodic pooling on the surface just beyond the point of breakup can occur until $We > 1500$, in which case the droplets contained enough residual momentum to carry them completely off the surface. It was shown that as We increased, the breakup radius increased due to the increased thin film momentum allowing it to spread further before surface tension caused breakup [13, 20, 21].

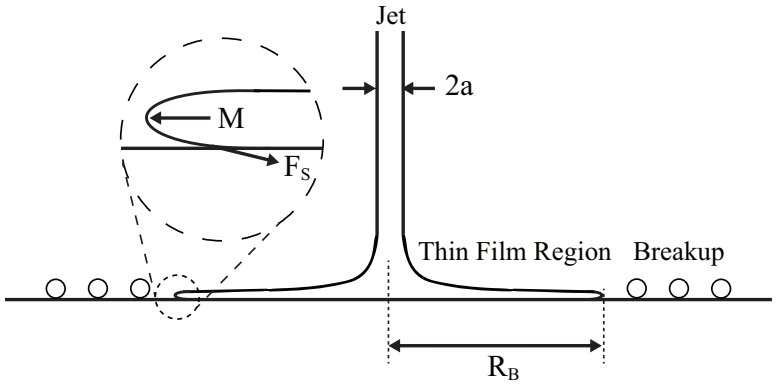

Figure 1.6: Diagram showing a side view of breakup of the thin film due to a laminar jet impinging on a SH surface. The dominant forces are shown at the location of breakup.

1.2.3 Droplet Impingement

The dynamics of a single droplet impinging on a hydrophilic surface are dominated by inertial, viscous, and surface tension forces. The impingement process is characterized by spreading of the droplet and rebounding capillary waves while the bulk of the droplet volume is stationary on the surface where impingement occurred. At high impact velocities, peripheral splashing can occur as well [22]. If a droplet impinges a hydrophobic or SH surface, the droplet retracts and can lift off the surface [23]. Figure 1.7 compares droplet impingement on a hydrophilic surface to that of a SH surface in a sequence of images. In the SH scenario where a micro or nano-structure is present, at the location of droplet impact the stagnation pressure may exceed the Laplace pressure, forcing fluid into the normally air filled cavities and pinning the droplet to the surface [24]. For large impact velocities, perturbations in the droplet symmetry cause fingering, or a non-uniform droplet perimeter. At even higher impact velocities the fingering protrusions break off, resulting in peripheral splashing. For SH surfaces, this splashing occurs at lower impact velocities than hydrophilic surfaces. Also, the droplet has been shown to experience differing shear stresses dependent on the surface microfeatures [25].

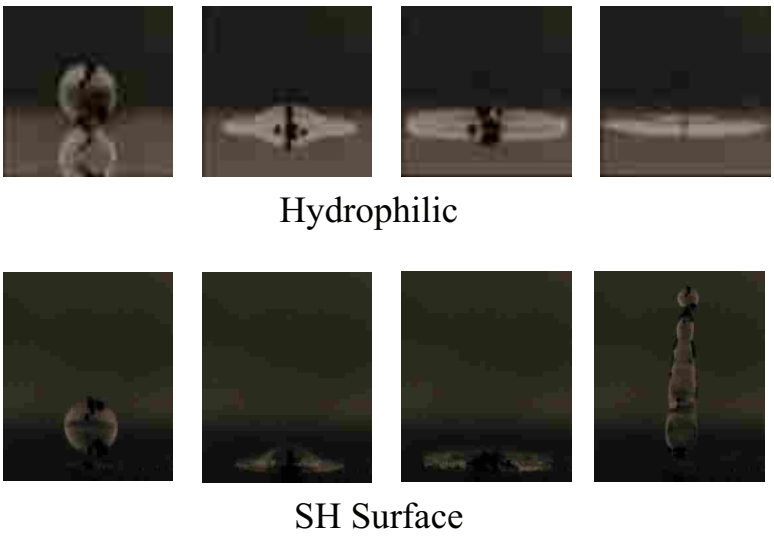

Figure 1.7: Sequence of images of a droplet impinging a smooth hydrophilic surface (Top) and a SH surface (Bottom).

When a droplet impacts a hydrophilic surface completely wetted by a liquid film, a remarkably different process ensues. This type of impingement is important in spraying applications, such as cooling or painting operations, as well as with falling rain. In these processes, a film of liquid is left behind by previous droplets. Spreading and splashing still occur, but a crown is formed at the leading edge and the thin film promotes increased splashing at the top of the crown, going upward. Cossali et al. [1] subdivided the process into four separate phases: droplet impact, crown formation, jet formation and break-up, and crown collapse (see Figure 1.8). A crown is formed at the leading edge of the spreading droplet and propagates outward while the crown height grows and then dissipates. The film eventually collapses inward and results in liquid jetting upward. If the momentum within the crown is sufficient, breakup of the crown, or splashing, occurs. Droplets produced by splashing separate from the top of the crown and have a significant vertical velocity component. Vander Wal et al. [26] investigated the effect of film thickness on the impingement dynamics by using the film thickness to droplet diameter ratio, $\delta = h/d$, to give two regimes. The first regime, $0.1 \leq \delta \leq 1$, exhibited two modes of splashing, prompt and delayed. The prompt splashing, which occurs immediately after impact with the film, has little effect on the impingement process due to the low amount of mass ejected. Delayed splashing is caused by instabilities in the rim of the crown causing jetting and breakup. The second regime, $1 \leq \delta \leq 10$, was characterized by reduction in the prompt splashing and inhibited delayed splashing which resulted in an

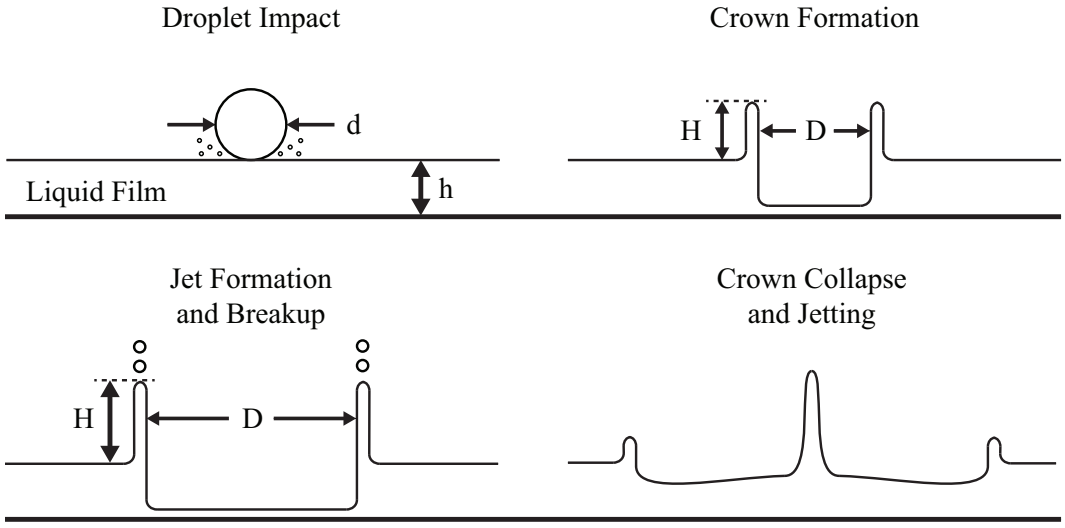

Figure 1.8: Diagram showing the temporal progression of a droplet impinging on a surface covered with a liquid film.

overall decrease in splashing. Alternatively, Cossali et al. [27] suggested two regimes based on a comparison with the surface roughness, R_a. A thin liquid film was described as $h \gg R_a$, where the surface had a weak influence. A very thin film was then for $h \approx R_a$, where the surface had a strong influence. The primary effect of increased surface roughness was an increase in splashing.

While most research has focused on the effects of splashing, there have been several experiments performed and models created to track the evolution of the crown properties of height, diameter, and thickness [1, 27–29]. There are some discrepancies, especially between models and experiments involving film thicknesses above $\delta = 0.29$ [1]. While the models indicate a significant increase in the crown height and diameter at any given time as the film thickness increases, experiments ranging from $\delta = 0.29 - 1.13$ have demonstrated a very weak influence with film thickness. Even so, all are in agreement that an increase in *We* results in an increase in the crown diameter at a given time and an increased maximum crown height.

1.2.4 Droplet Train

A droplet train is a series of fluid droplets which move in sequence along the same trajectory. In practice, droplets will not usually be uniform in size, trajectory, or frequency of impact. Spray cooling, for instance, will have many fluid droplets impinging randomly across a surface, which has been shown by Sivakumar [30] to give differing results than a uniform droplet train. However, an investigation into the characterization of the impingement process can be made, and in the case of certain printing applications, these droplet trains do accurately describe the process as the ink droplets are guided precisely to certain locations in order to gain high resolution. As each droplet hits the surface they follow the general dynamics of a single droplet hitting a surface with a thin film of the same fluid. If the frequency of impinging droplets is low, then the crown collapses before each subsequent impingement and remains as if it were a single droplet. By increasing the frequency, subsequent droplets will impinge before the crown collapses as shown in Figure 1.9. In this case, each droplet impinges on the thin film created by the previous droplet. When this occurs on a hydrophilic surface, a quasi-steady crater is maintained by the periodic outward momentum of each crown. [31].

Since breakup within the crown rim is not affected by the previous or subsequent crowns, splashing dynamics are usually considered the same as for a single droplet impinging a thin film.

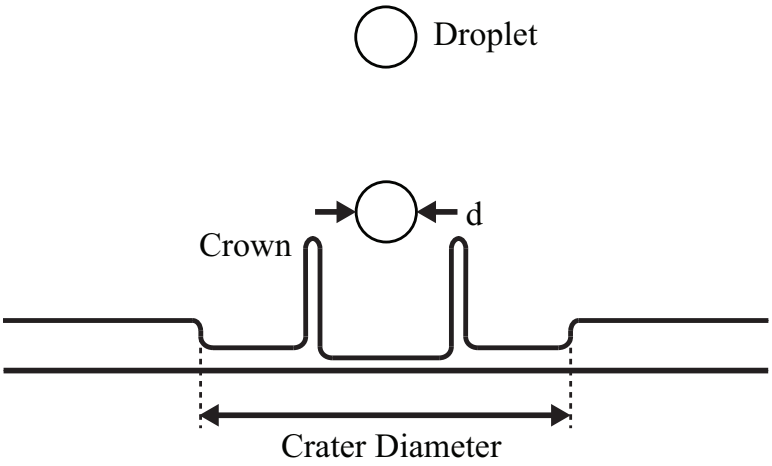

Figure 1.9: Diagram showing a droplet train impinging on a surface.

Thus the relations described previously are used for both. There is a potential difference due to the presence of the crater in droplet train impingement which was not accounted for in previous work. Yarin and Weiss, for example, used a curved surface to keep any liquid from building up [28]. While no study has done so for a droplet train, jet impingement with an imposed film thickness has shown that the hydraulic jump, or crater, will decrease as the film thickness increases [20, 21]. If this occurred for a droplet train, it may interfere with the splashing dynamics.

A combination of a droplet train model and experiments were performed by Yarin and Weiss [28]. They predicted the onset of splashing using the following equation:

$$\varepsilon = (\alpha \nu^{1/2} f^{2/3})/(\rho V_0^4) \tag{1.2}$$

Where α is the surface tension, ν the kinematic viscosity, f the droplet frequency, ρ the fluid density, and V_0 the droplet impact velocity. It was determined that splashing occurs when ε is less than a nominal value of 18^{-4}. Yarin and Weiss also experimentally determined the splashing threshold for a range of frequencies and impact velocities. Doing so, they found a correlation for the splashing threshold as $Ca = C\lambda^{3/4}$, where $Ca = (\mu V)/\sigma$ is the Capillary number, $\lambda = (\nu/f)^{1/2}\sigma/(\rho\nu)^2$, and C is a constant with a weak dependence on surface roughness. For a given λ, splashing occurred for values of Ca above the splashing threshold, and values below resulted in deposition (no splashing). As λ increased, the value of Ca required to cause splashing decreased.

1.3 Thesis Organization

This thesis consists of three stand-alone papers which explore the dynamics of droplet and jet impingement on SH surfaces. Each will describe a different dynamic and how it compares with and differs from the more commonly studied hydrophilic surface dynamics. The first, Chapter 2, identifies and analyzes a transition regime within jet impingement on a superhydrophobic surface due to a varying imposed downstream depth. This transition occurs between regimes of thin film breakup on a free surface and formation of a classical hydraulic jump due to an imposed downstream depth. It is characterized by the presence of both thin film breakup and a free hydraulic jump. The range over which the transition occurs and its relation to previous work is reported. Chapter 3 then reports the crown dynamics of a droplet impinging a superhydrophobic surface coated with a liquid film, with comparisons to a smooth hydrophilic surface. Chapter 4 gives the results of droplet train impingement experiments on a superhydrophobic surface. Observations of the dynamics are made along with noted anomalies. A comparison of splashing dynamics is made to previous experiments on hydrophilic surfaces. Measured breakup diameter data is examined and compared between post and rib microfeatures. The breakup diameter for droplet train impingement is then compared to that of jet impingement. The thesis results are then summarized in Chapter 5.

CHAPTER 2. JET IMPINGEMENT ON SUPERHYDROPHOBIC SURFACES AND THE TRANSITION FROM BREAKUP TO HYDRAULIC JUMP FORMATION

2.1 Abstract

When a jet impinges on a hydrophilic surface or a superhydrophobic (SH) surface with an imposed downstream depth, a hydraulic jump forms. If a jet impinges on an unimmersed SH surface, thin film breakup occurs. Here we explore the transitional regime between thin film breakup and a classical hydraulic jump for jet impingement on a SH surface. Silicon wafers were utilized with a surface topology of an array of microposts 12-16 μm tall, a pitch of 16.5 μm, and had a cavity fraction, F_c, of about 87%. A hydrophobic coating was applied, achieving contact angles of 140 to 150 degrees. It is shown that for a range of imposed downstream depths, either thin film breakup, a hydraulic jump, or both can occur. Experiments were performed for a range of three Reynolds numbers from 1.9×10^4 to 2.2×10^4 (based on the volume flow rate). The range of *Re* was limited by insufficient momentum and jet collapse at low *Re* and surface robustness at high *Re*. For all *Re*, the transition was characterized by a reduction in hydraulic jump radius as downstream depth increased until reaching the jet breakup radius. For larger Reynolds numbers, the downstream depths over which the transition occurred was greater.

2.2 Introduction

2.2.1 Superhydrophobicity

Fluid dynamics involving superhydrophobic (SH) surfaces has been of great interest in recent research. This is due to the manner in which these surfaces alter the fluid flow compared to smooth hydrophilic and even hydrophobic surfaces. SH surfaces are characterized by their high contact angle, $\theta > 120°$, as shown in Figure 2.1. This material property is ideal in situations requiring reduced liquid/surface contact area. In order to achieve such high contact angles, a

hydrophobic coating must be applied to a microstructured surface if it is not natively hydrophobic. The microstructure enhances the hydrophobicity of the surface when the fluid sits above the air cavities between the microstructure (Cassie-Baxter state). If the pressure exceeds the Laplace pressure, defined as $\Delta P = \sigma(1/R_1 + 1/R_2)$, where σ is the surface tension and R_1 and R_2 are the radii of curvature of the meniscus, then the fluid penetrates the cavities. When the surface wets in this fashion, it is termed the Wenzel state and the contact angle is lower [5].

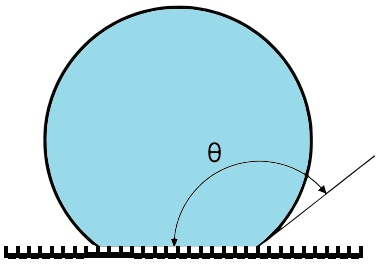

Figure 2.1: Drawing of a droplet of water sitting on a SH surface. The contact angle, θ, is the angle from the surface in contact with the water to the liquid surface extending outward.

The lotus leaf is often referred to as a prime example of a SH surface, where the leaves use hydrophobic waxes covering a micro-topography of papillae [3]. There are various approaches to duplicate this phenomenon. Etching silicon or growing carbon nanotubes are common methods developed to generate micro, or nano, structures [4]. These methods can be utilized to create random or carefully patterned microstructures such as posts or ribs. Other methods, such as using abrasives or a spray-on coating, will only allow for randomized microstructures. Natively hydrophilic surfaces (surfaces with $\theta < 90°$) are often coated with a hydrophobic coating (such as wax or Teflon®) to render them SH. These surfaces have been shown to decrease condensation buildup on condensers by allowing water to roll or even jump off surfaces [14]. When in the Cassie-Baxter state, SH surfaces display an apparent slip velocity near the surface due to negligible shear at the water-air interface over the cavities [7–9]. The slip is a function of the distance between adjacent microstructures (pitch) and the fraction of water in contact with air (cavity fraction). An increase in either of these surface properties results in an increase in the slip [10]. This decreases the friction

drag, which is desirable in microchannels and microfluidic devices where viscous effects from the wall require large pressure gradients to drive the flow [11].

2.2.2 Jet Impingement

Jet impingement is a common process, especially in many heat transfer operations. Because of the self cleaning and liquid removal properties, SH surfaces may be useful in these applications. While the effects of superhydrophobicity have been examined for jet impingement, we focus here on hydraulic jump dynamics due to a transition between an unsubmerged and a completely submerged SH surface. When a jet impinges on a surface, it spreads out into a thin film as shown in Figure 2.2. The thin film radial velocity decreases as it moves outward due to viscous drag and radial spreading. The fluid momentum for a thin slice of the spreading film is defined as $M = \int \rho V^2 dA$, where ρ is the density, V is the velocity profile across the thickness of the film, and A is the cross-sectional area (spanning the circumferential length and film thickness). Once the velocity decreases sufficiently, M will reach a balance with the hydrostatic force, F_H, of a resulting or imposed downstream depth [16]. At this radius, R_H, a hydraulic jump is created where the surface height of the liquid becomes that of the downstream depth, h. Surface tension, F_S, can also play a role, acting radially inward from the hydraulic jump. Bush and Aristoff showed that surface tension will decrease the hydraulic jump radius, but the effect is diminished as the jump radius increases [17]. Prince et al. modeled slip on the surface in the thin film region and found the presence of slip resulted in increased momentum, which increased the jump radius. This effect was more

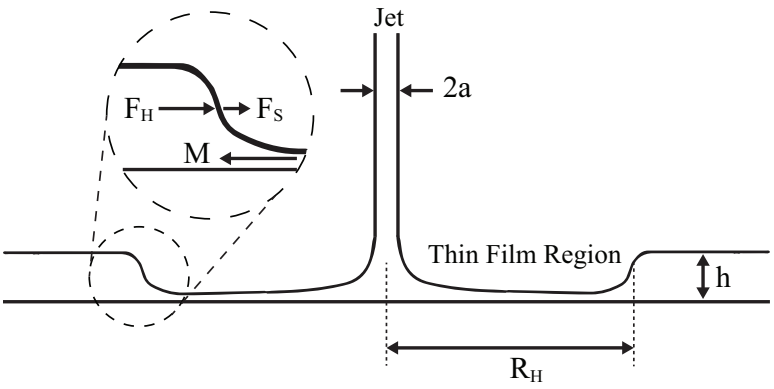

Figure 2.2: Diagram showing a side view of hydraulic jump formation due to a laminar jet impinging on a surface. The dominant forces are shown at the location of the hydraulic jump.

pronounced for greater jump radii as slip had greater area over which to exert influence [18]. The model used by Prince et al. [19] has been compared to jet impingement on SH surfaces patterned with microribs [20]. The model showed good agreement to the data with a maximum deviation of 8% in the direction of the ribs and 10-16% in the direction transverse to the ribs. The error in the transverse direction was attributed to utilizing an inaccurate value of slip in the transverse direction, but was not explored further. Johnson [20] and Prince et al. [19] found that altering the pattern on the surface (e.g., ribs or posts) can change the resulting shape of the hydraulic jump due to the difference in slip in each direction. Both also showed that as the downstream depth was increased or the Weber number ($We = \rho V^2 d/\sigma$) decreased, the hydraulic jump diameter decreased due to an increase in the hydrostatic force compared to the fluid momentum.

It has been demonstrated that without an imposed downstream depth, jet impingement on a hydrophobic or SH surface can result in breakup of the thin film instead of a hydraulic jump [20, 21]. Figure 2.3 shows jet impingement and thin film breakup on a SH surface. In this case, the high contact angle results in a significant surface tension force pulling inward. This causes the thin film on the surface to break up into droplets due to surface tension forces at a critical location denoted as the breakup radius, R_B. At this point, the force due to momentum, F_m, balances with the surface tension, F_S. Johnson [20] and Maynes et al. [21] demonstrated that at a Weber number of about 1000, breakup of the thin film into droplets began occurring. At this condition there is enough momentum to generate droplets that continue to move outward. Otherwise, the fluid flows outward as filaments or simply builds up on the surface. Droplet coalescence and periodic

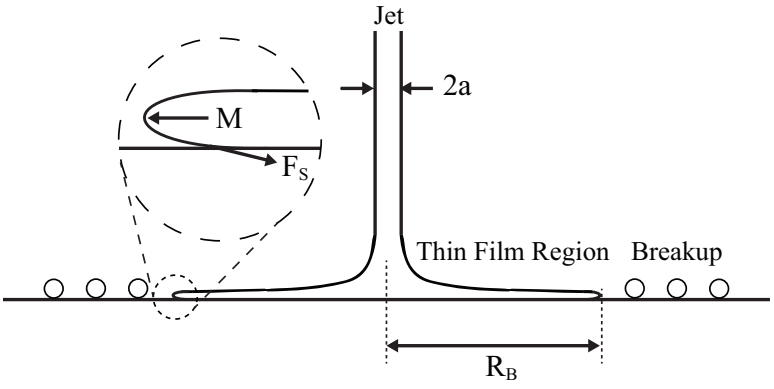

Figure 2.3: Diagram showing a side view of breakup of the thin film due to a laminar jet impinging on a SH surface. The dominant forces are shown at the location of breakup.

pooling on the surface just beyond the point of breakup can occur until $We > 1500$, in which case the droplets contained enough residual momentum to carry them completely off the surface. It was shown that as We increased, the breakup radius increased due to the increased thin film momentum, allowing it to spread further before surface tension caused breakup [13, 20, 21].

The dynamics of both the hydraulic jump and thin film breakup have been explored. However, when a downstream depth is imposed, droplets moving outward may create a hydraulic jump which is unattached to the thin film. This combined breakup to hydraulic jump situation is investigated here.

2.3 Methods

In order to perform the experiments, SH surfaces with a patterned microstructure were produced in-house. Also, a setup was designed and built in order to produce a water jet which would impinge on the SH surface. The setup included a method for maintaining a downstream depth as well as collect needed measurements.

2.3.1 SH Surface Fabrication

All surfaces were fabricated from 4 inch diameter silicon wafers, and existing photolithographic methods were utilized to make a grid pattern of round microposts on the wafers. First, the silicon wafers were coated with a negative photoresist. Using an aligner, a mask was positioned on top of a wafer and exposed. The wafers were subsequently developed so as to remove the unexposed photoresist resulting in the desired pattern. The wafers were then etched using deep reactive-ion etching (DRIE) and the remaining photoresist subsequently removed. As seen in Figure 2.4 the microposts were cylindrical structures nominally 12-16 μm tall, a pitch of 16.5 μm, and a cavity fraction F_c of about 87%. In order to allow good adhesion of a hydrophobic coating, the surfaces were coated with a thin chromium layer (100 nm) using a thermal evaporator. These surfaces were then coated with a thin layer of Teflon® (<200 nm) which, along with the microstructure, render the surfaces superhydrophobic. The static contact angle, θ, for all surfaces was nominally 165°, with receding and advancing contact angles of nominally 140° and 168° respectively.

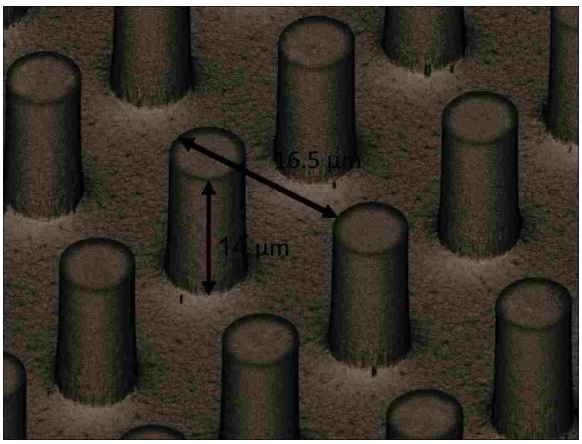

Figure 2.4: SEM images of the microscale post surface topography as designed and created with common photolithography techniques on a silicon wafer.

2.3.2 Experimental Setup and Measurements

As shown in Figure 2.5, water was pressurized in a tank and connected via a valve to a nozzle. The exiting water flow was directed vertically downward, impinging on the wafer placed in a flat position below the nozzle. The distance of the nozzle above the wafer was such that there were negligible effects from gravity and no Rayleigh instabilities (breakup of the jet) were observed. The setup allowed for control of the flow through a needle valve and measurement of flow speeds using an in-line flow meter. The jet radius, a, was controlled by the nozzle size, and was constant at 0.6 *mm* for all experiments. The wafer was placed in a reservoir with the downstream depth initially set slightly below the depth required to collapse a hydraulic jump, as discussed in Section 2.4.1. Through the course of the experiment, the reservoir would fill gradually, thus increasing the downstream depth. This continued until a classical hydraulic jump was achieved.

A CCD camera was oriented above the wafer at an angle relative to the plane of the wafer to provide a nearly top down view. The camera captured video at 30 fps throughout the experiment of the breakup and hydraulic jump. The radii of breakup and the hydraulic jump were then measured throughout each video. Because of thin film breakup, the downstream depth is disconnected from the thin film region and cannot affect breakup location. Thus, the breakup radius remained constant for each test and the measurements were averaged over several frames to obtain a single value. The hydraulic jump radius varied throughout the experiment, and was measured so that each data point corresponded to a single frame captured at a known time. By measuring the initial and final

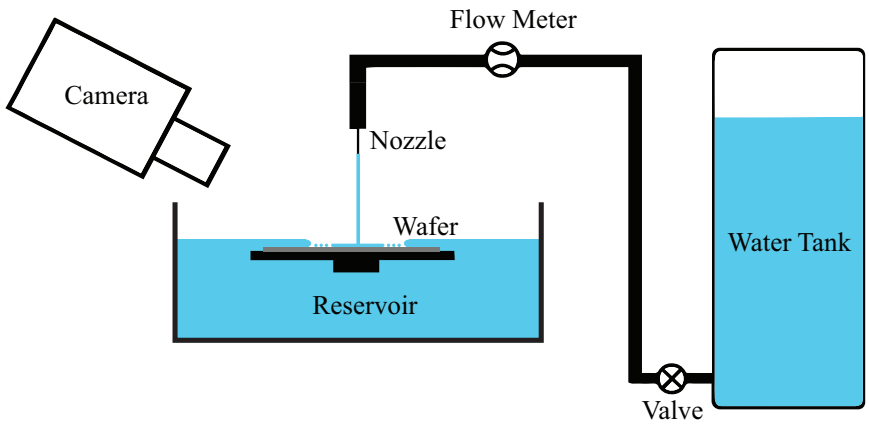

Figure 2.5: Setup of apparatus used to perform jet impingement experiments.

downstream depths, and assuming a linear increase in height within the reservoir, the height at any given time was determined. The hydraulic jump radius can then be found as a function of downstream depth. The change in downstream depth was nominally 1-1.6 mm and changed at a rate of nominally 36-48 μm/s.

The measured breakup radius, R_B, and hydraulic jump radius, R_F, vary with the fluid's impingement velocity, downstream height, viscosity, and surface tension. This paper only utilizes changes in impingement velocity by altering the volume flow rate, Q, and changes in the downstream height, h. Q was varied from 0.18 to 0.21 gpm. Reynolds number was defined as $Re = Q/(\nu a)$, where ν is the kinematic viscosity. The resulting variation in Re was from 1.9×10^4 to 2.2×10^4 over four tests, with the $Re = 2.2 \times 10^4$ case performed twice.

The measurement uncertainty for the downstream depth was determined to be less than 2% while for the radii the maximum uncertainty was 3.5%. The repeatability was determined with the replication of the test at $Re = 2.2 \times 10^4$, resulting in a maximum uncertainty of 14.5%, and an average uncertainty of 5.3%. This error is largely due to the natural fluctuations in the hydraulic jump radius. A fit of the data was utilized which somewhat mitigated the fluctuations.

2.4 Results

2.4.1 Critical Downstream Depth

Without an impinging jet, water will either remain completely off or cover the surface due whether the downstream depth is small or large. In Figure 2.6 is shown a schematic of the forces acting on the liquid and an image of the liquid as it collapses inward on a SH surface. Due to the high contact angle, the force of surface tension is directed radially outward as depicted by F_s. Also, due to the imposed downstream depth, a hydrostatic force, F_H, is directed radially outward. Balancing the hydrostatic and surface tension forces gives an equation for the critical downstream depth, $h = \sqrt{2\sigma(1-cos(\theta))/\rho g}$, at which the liquid will collapse onto the surface covering it completely. For the surface shown, with $\theta = 165°$, this results in a downstream depth of 5.12 mm, above which the liquid will immediately collapse. Experiments on the SH surface gave a depth of nominally 5 mm, which is in good agreement. This height is a lower bound, and at lower values the liquid will pull completely off the wafer surface.

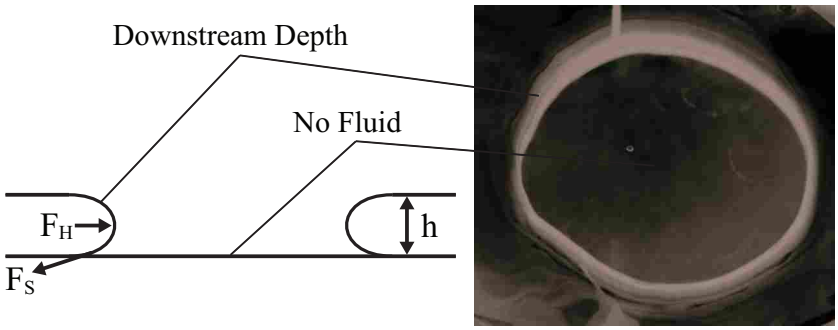

Figure 2.6: Diagram and image showing an imposed downstream depth on a SH micropost surface. The center of each is void of water. The image was taken as the jump began to collapse due to the downstream depth.

2.4.2 Transition Regime

If a jet is impinging on a SH surface, greater downstream depths can be achieved before the liquid collapses due to the added momentum of the fluid. Specifically, we look at the transition

regime where the thin film on the SH surface breaks up and the spreading droplets balance with the downstream depth. This transition is shown in Figure 2.7 displaying both breakup and the hydraulic jump. In this instance, the hydraulic jump is not attached to the thin film. It is characterized by both a breakup radius, R_B and a hydraulic jump radius, R_F. At breakup, there is a balance between the surface tension, F_S, and the momentum, $F_B = \int \rho V_B^2 dA$, just as in Figure 2.3. At the hydraulic jump, a balance between the surface tension, F_S, and hydrostatic force, F_H, is the same as Figure 2.6, but a momentum term, $M = \int \rho V^2 dA$, from the droplets is added. As the downstream depth increases above the critical height, the downstream fluid encroaches on the droplet region. Further increasing causes the downstream depth to completely engulf the droplets and a classical hydraulic jump occurs with the surface completely submerged.

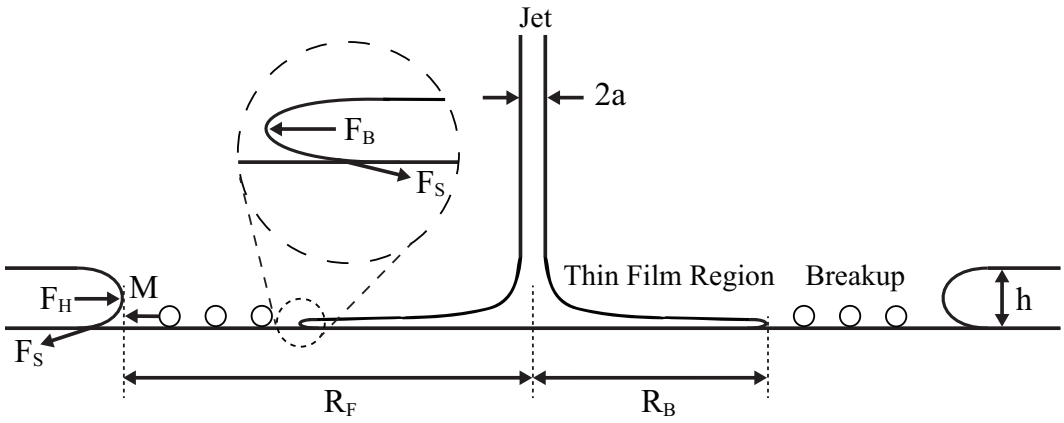

Figure 2.7: Side view diagram showing breakup and hydraulic jump formation due to a laminar jet impinging on a superhydrophobic surface. The dominant forces are shown at the location of breakup and the hydraulic jump.

A series of images consisting of three regimes of flow are shown in Figure 2.8. The jet is centered in the pictures with the thin film spreading out from the point of impingement. The first region (a) is before the transition, where the downstream depth is insufficient to form a hydraulic jump on the surface. The thin film breaks up and the resultant droplets spread freely radially outward. The last region (c) is after the transition where a classic hydraulic jump forms. The center image (b) shows the transition regime with the breakup radius and hydraulic jump showing as concentric circles. Note the hydraulic jump is not perfectly circular. This deviation is due to the

Figure 2.8: Sequence of images from CCD of jet impingement on a SH surface. Displayed are the three regimes of flow. Before the transition (a) only breakup can be seen and after (c) only a classic hydraulic jump occurs. The transitional regime (b) displays both breakup and a hydraulic jump.

irregularity of the incidence of droplets produced by the thin film breakup on the hydraulic jump. The greatest source of variation found throughout the experiments was in these natural fluctuations.

There exists a lower bound on *Re* required to produce both breakup and the hydraulic jump. Below *Re* of nominally 1.6-1.8$\times 10^4$ the momentum of the droplets produced by thin film breakup is drastically reduced, such that there is no longer enough momentum to prevent the hydraulic jump from collapsing. When this happens, no transition occurs. There was also a restriction in using higher *Re* as the hydrophobic coating was quickly eroded away at *Re* much higher than 2.2×10^4.

While all data reported here was gathered using SH surfaces with a post microstructure, video was taken using a rib microstructure for further insight. Figure 2.9 shows an image of the transition regime for a jet impinging on a rib SH surface, having both thin film breakup and a hydraulic jump. In the image, the hydraulic jump has collapsed in the transverse direction (perpendicular to the ribs) such that the combined breakup and hydraulic jump only exists in the longitudinal direction (parallel to the ribs). The thin film region is somewhat elongated and the hydraulic jump is greatly elongated in in the longitudinal direction due to the redirection of the momentum in the thin film caused by the ribs. Because of the limit on wafer size and the large elongation in hydraulic jump, it was not possible to obtain data unaffected by the wafer edges on these ribbed surfaces.

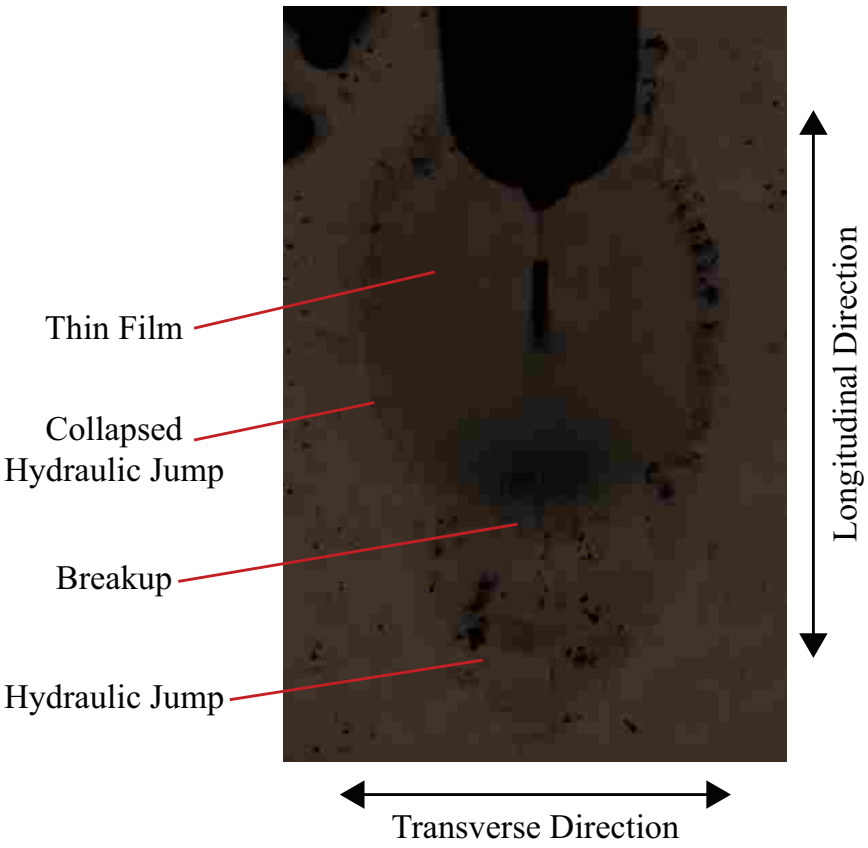

Figure 2.9: An image of the transition regime containing both breakup and a hydraulic jump for a jet impinging on a rib SH surface.

2.4.3 Transition Radius Data

The ratio of the jump radius to jet radius, R/a, for each tested Re is plotted as a function of the normalized downstream depth, h/a in the left plot of Figure 2.10. The right plot in the figure displays the data for $Re = 2.0 \times 10^4$. In this plot, the wafer radius is denoted by an x overlain on a solid line. The dashed vertical line is the downstream depth, h/a, at which a hydraulic jump collapses without jet impingement present. The measured average breakup radius, R_B/a, is the line denoted by the open square and is constant as it is a function of Re only. The line denoted with an open circle represents the analytical model by Prince et al. [18] of the hydraulic jump location, R_H/a, for a given downstream depth. This model estimates the hydraulic jump for a submerged surface with slip at the surface boundary. The hydraulic jump radius data, R_F/a, is represented as solid circles. The transition for this Re ranges from $h/a = 8.9 - 9.8$ which corresponds to a change in h of nominally 0.6 mm. For downstream depths below this, the data remains at the wafer radius,

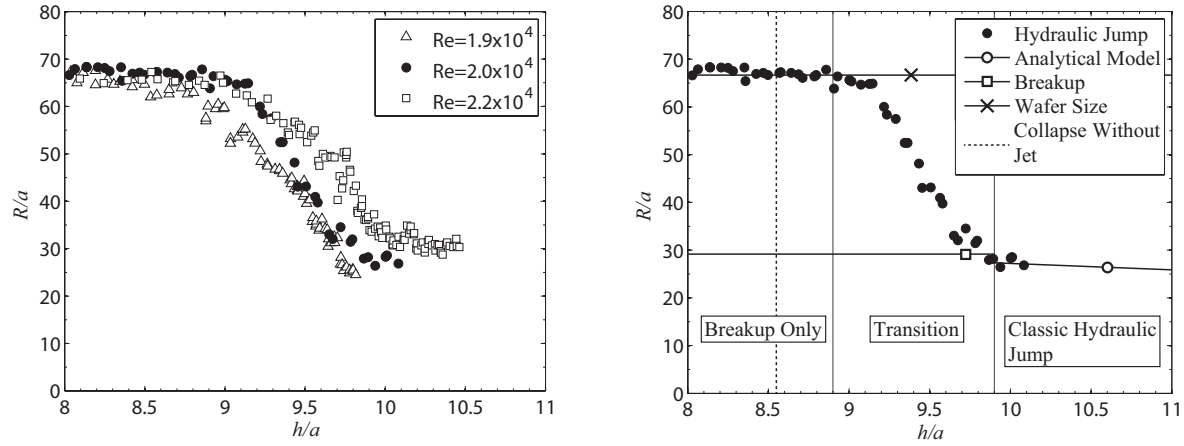

Figure 2.10: Nondimensional jump radius, R/a, over the duration of an experiment as a function of the nondimensional downstream depth, h/a. (Left) Data for each of the three *Re* tested. (Right) Data for $Re = 2.0 \times 10^4$, along with the three regimes of flow are shown along with the wafer size, breakup radius, and analytical model radius. The critical downstream depth at which the hydraulic jump collapses without a jet is also shown.

and only breakup occurs on the surface. The hydraulic jump stays off the surface until reaching the transition and the hydraulic jump radius begins to decrease. It's important to note that because of the outward momentum of the droplets, the transition starts at a larger downstream depth than the collapse height when no jet impingement is present. As the downstream depth increases, the hydraulic jump collapses to slightly under the breakup radius. At this point a classical hydraulic jump is formed and the transition ends. For downstream depths greater than this transition region, the data follow the analytical model for a classical hydraulic jump.

A linear fit of the hydraulic jump radius data, in the transition region only, is shown in Figure 2.11, solid lines with closed symbols, for all three *Re* explored. Again the breakup radius, dashed lines with open symbols, and analytical model radius, solid line with open symbols, as described for Figure 2.10, are plotted at each *Re* for reference. There are a few main observations. First note the breakup radius increases with increasing *Re* as expected from previous work [13,21]. Second the hydraulic jump radius increases with increasing *Re*. At a given downstream depth, the only difference is in the momentum of the jet which is then transfered throughout. Thus, the increased jump radius is attributed to the increase in momentum the droplets carry from the thin film breakup to the hydraulic jump. There is also an increase in the radius at which the hydraulic jump collapses to the radius of breakup. The linear fit for both *Re* of 1.9×10^4 and 2.0×10^4 had R-

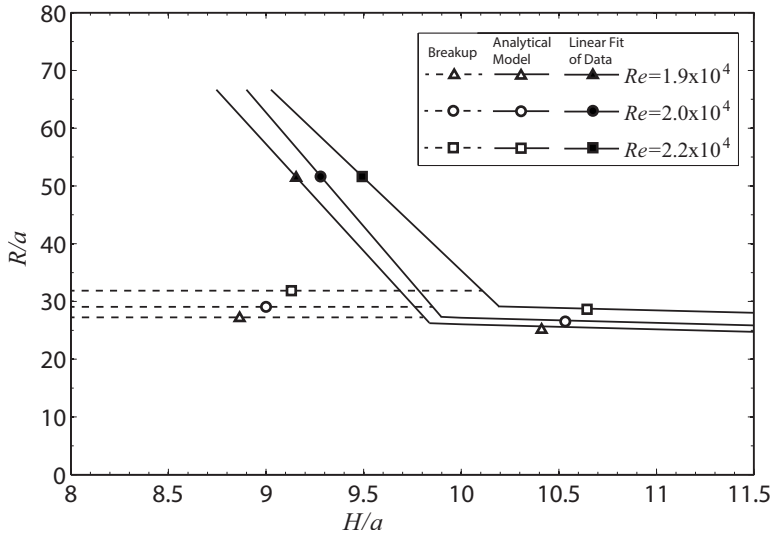

Figure 2.11: Linear fits of nondimensional jump radius, R/a, are plotted for the transition regime as a function of nondimensional downstream depth, h/a. Shown are *Re* of 1.9×10^4, 2.0×10^4, and 2.2×10^4. The breakup radius and the analytical model radius are plotted as well.

squared values of 0.95, while the fit for *Re* of 2.2×10^4 had and R-squared value of 0.92. Table 2.1 presents the range of h/a for each region of flow and the slope and intercept of the fit within the transition region. From the relatively small range over which the transition occurs, a change in h/a of near unity, we can conclude that the impact of the droplets leaving the breakup radius is relatively small when compared to the hydrostatic force imposed by the downstream depth. The slight variation in slope of each of the lines may be attributed to error, but the sharp negative trend in the slope of is consistent. For *Re* above what was tested, the same trends are expected to continue. However, lower *Re* value the transition occurs abruptly due to reduced momentum allowing immediate collapse of the hydraulic jump.

Table 2.1: Table listing the ranges of downstream depth for each region (breakup with the hydraulic jump off the wafer, within the transition, and after collapse with a classical hydraulic jump). Also, the slope and intercept is given for the transition region.

Re	Breakup	Transition Regime			Classical Hydraulic Jump
	Range	Range	Slope	Intercept	Range
1.9x10^4	h/a<8.75	8.75<h/a<9.87	-37	390	h/a>9.87
2.0x10^4	h/a<8.90	8.90<h/a<9.91	-39	417	h/a>9.91
2.2x10^4	h/a<9.03	9.03<h/a<10.17	-32	356	h/a>10.17

2.5 Conclusion

In this research, the dynamics of fluid flow over a SH surface due to jet impingement has been explored over a specific transition region between the well known thin film breakup and a classical hydraulic jump. Due to changes in downstream depth, a region where both phenomenon occur is discovered which has not been previously explored. Experiments involving three different *Re* numbers from 1.9-2.2$\times 10^4$ were performed to track the hydraulic jump as it collapsed. The transition occurred over a range of downstream depths, h/a, of nominally 1. For a given downstream depth during the transition, the hydraulic jump radius is greater for larger *Re*. Also, as *Re* increases, the radius at which the hydraulic jump reaches the breakup radius increases. A transition was not observed for *Re* below the minimum tested value 1.9×10^4, but is expected to occur for values above the maximum tested *Re* of 2.2×10^4.

CHAPTER 3. DROPLET IMPINGEMENT ON A LIQUID COATED SUPERHYDROPHOBIC SURFACE

3.1 Abstract

When a droplet impinges on a surface covered with a liquid film, a thin liquid wall, or crown, forms and propagates outward. Here a comparison of this crown dynamic was made for smooth hydrophilic surfaces and superhydrophobic (SH) surfaces patterned with post or rib microfeatures. The height of the features for both was nominally 12-16 μm and the spacing for the post and ribbed surfaces were 16.5 μm and 32 μm respectively. The setup used a syringe to expel a droplet of water from a specified height which then impinged on a surface covered with a film of water. Experiments were performed over a Weber number, *We*, range of 350 to 1250. Due to the high contact angle of the SH surfaces, a relatively thick film ($h \approx 5$ mm) of water was required to maintain a film. This resulted in negligible differences between the surfaces utilized.

3.2 Introduction

3.2.1 Superhydrophobicity

Fluid dynamics involving superhydrophobic (SH) surfaces has been of great interest in recent research. This is due to the manner in which these surfaces alter the fluid flow compared to smooth hydrophilic and even hydrophobic surfaces. SH surfaces are characterized by their high contact angle, $\theta > 120°$, as shown in Figure 3.1. This material property is ideal in situations requiring reduced liquid/surface contact area. In order to achieve such high contact angles, a hydrophobic coating must be applied to a microstructured surface if it is not natively hydrophobic. The microstructure enhances the hydrophobicity of the surface when the fluid sits above the air cavities between the microstructure (Cassie-Baxter state). If the pressure exceeds the Laplace pressure, defined as $\Delta P = \sigma(1/R_1 + 1/R_2)$, where σ is the surface tension and R_1 and R_2 are the

radii of curvature of the meniscus, then the fluid penetrates the cavities. When the surface wets in this fashion, it is termed the Wenzel state and the contact angle is lower [5].

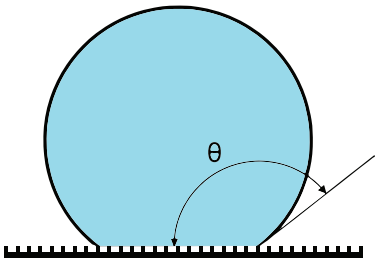

Figure 3.1: Drawing of a droplet of water sitting on a SH surface. The contact angle, θ, is the angle from the surface in contact with the water to the liquid surface extending outward.

The lotus leaf is often referred to as a prime example of a SH surface, where the leaves use hydrophobic waxes covering a micro-topography of papillae [3]. There are various approaches to duplicate this phenomenon. Etching silicon or growing carbon nanotubes are common methods developed to generate micro, or nano, structures [4]. These methods can be utilized to create random or carefully patterned microstructures such as posts or ribs. Other methods, such as using abrasives or a spray-on coating, will only allow for randomized microstructures. Natively hydrophilic surfaces (surfaces with $\theta < 90°$) are often coated with a hydrophobic coating (such as wax or Teflon®) to render them SH. These surfaces have been shown to decrease condensation buildup on condensers by allowing water to roll or even jump off surfaces [14]. When in the Cassie-Baxter state, SH surfaces display an apparent slip velocity near the surface due to negligible shear at the water-air interface over the cavities [7–9]. The slip is a function of the distance between adjacent microstructures (pitch) and the fraction of water in contact with air (cavity fraction). An increase in either of these surface properties results in an increase in the slip [10]. This decreases the friction drag, which is desirable in microchannels and microfluidic devices where viscous effects from the wall require large pressure gradients to drive the flow [11].

3.2.2 Droplet Impingement

The dynamics of a single droplet impinging on a hydrophilic surface are dominated by inertial, viscous, and surface tension forces. The impingement process is characterized by spreading of the droplet and rebounding capillary waves while the bulk of the droplet volume is stationary on the surface where impingement occurred. At high impact velocities, peripheral splashing can occur as well [22]. If a droplet impinges a hydrophobic or SH surface, the droplet retracts and can lift off the surface [23]. In the SH scenario where a micro or nano-structure is present, at the location of droplet impact the stagnation pressure may exceed the Laplace pressure, forcing fluid into the normally air filled cavities and pinning the droplet to the surface [24]. For large impact velocities, perturbations in the droplet symmetry cause fingering, or a non-uniform droplet perimeter. At even higher impact velocities the fingering protrusions break off, resulting in peripheral splashing. For SH surfaces, this splashing occurs at lower impact velocities than hydrophilic surfaces. Also, the droplet has been shown to experience differing shear stresses dependent on the surface microfeatures [25].

When a droplet impacts a hydrophilic surface completely wetted by a liquid film, a remarkably different process ensues. This type of impingement is important in spraying applications, such as cooling or painting operations, as well as with falling rain. In these processes, a film of liquid is left behind by previous droplets. Spreading and splashing still occur, but a crown is formed at the leading edge and the thin film promotes increased splashing at the top of the crown, going upward. Cossali et al. [1] subdivided the process into four separate phases: droplet impact, crown formation, jet formation and break-up, and crown collapse (see Figure 3.2). A crown is formed at the leading edge of the spreading droplet and propagates outward while the crown height grows and then dissipates. The film eventually collapses inward and results in liquid jetting upward. If the momentum within the crown is sufficient, breakup of the crown, or splashing, occurs. Droplets produced by splashing separate from the top of the crown and have a significant vertical velocity component.

Vander Wal et al. [26] investigated the effect of film thickness on the impingement dynamics by using the film thickness to droplet diameter ratio, $\delta = h/d$, to give two regimes. The first regime, $0.1 \leq \delta \leq 1$, exhibited two modes of splashing, prompt and delayed. The prompt splashing, which occurs immediately after impact with the film, has little effect on the impinge-

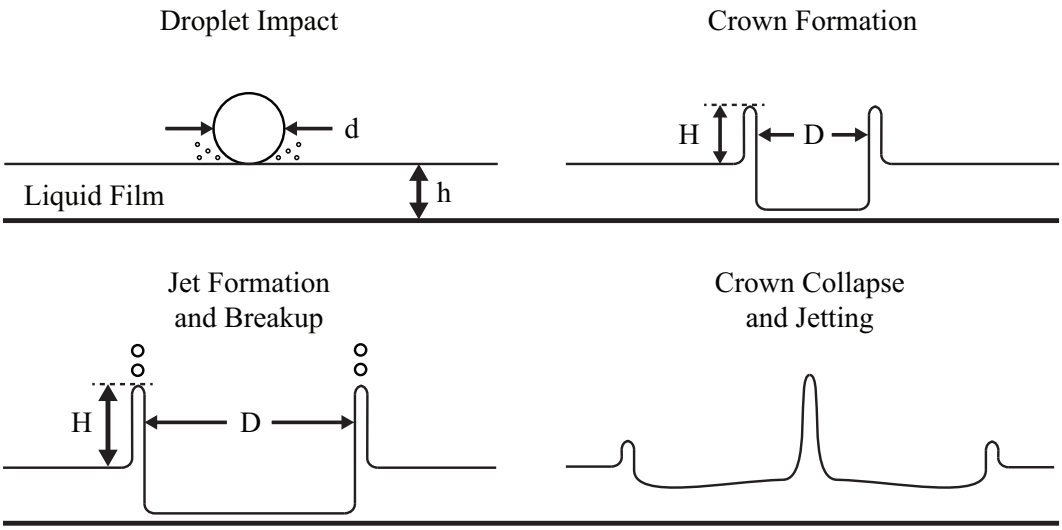

Figure 3.2: Diagram showing the temporal progression of a droplet impinging on a surface covered with a liquid film.

ment process due to the low amount of mass ejected. Delayed splashing is caused by instabilities in the rim of the crown causing jetting and breakup. The second regime, $1 \leq \delta \leq 10$, was characterized by reduction in the prompt splashing and inhibited delayed splashing which resulted in an overall decrease in splashing. Alternatively, Cossali et al. [27] suggested two regimes based on a comparison with the surface roughness, R_a. A thin liquid film was described as $h \gg R_a$, where the surface had a weak influence. A very thin film was then for $h \approx R_a$, where the surface had a strong influence. The primary effect of increased surface roughness was an increase in splashing.

While most research has focused on the effects of splashing, there have been several experiments performed and models created to track the evolution of the crown properties of height, diameter, and thickness [1, 27–29]. There are some discrepancies, especially between models and experiments involving film thicknesses above $\delta = 0.29$ [1]. While the models indicate a significant increase in the crown height and diameter at any given time as the film thickness increases, experiments ranging from $\delta = 0.29 - 1.13$ have demonstrated a very weak influence with film thickness. Even so, all are in agreement that an increase in *We* results in an increase in the crown diameter at a given time and an increased maximum crown height.

The dynamics of droplet impingement onto a hydrophilic surface covered by a thin film have been explored, and experiments have been performed using various surface features. Recently there is an increasing desire to utilize SH surfaces in environments, such as spray cooling

operations, where surfaces are subjected to droplet impingement. So far, no research has been accomplished to characterize the effect of droplet impingement on liquid coated SH surfaces. A comparison of the crown dynamics of a smooth hydrophilic surface to patterned SH surfaces is made here.

3.3 Methods

In order to perform the experiments, SH surfaces with a patterned microstructure were produced in-house. Also, a setup was designed and built in order to produce a water droplet which would impinge on the desired surface. The setup included a method for maintaining a downstream depth as well as collect measurements of the crown evolution.

3.3.1 Surface Fabrication

The SH surfaces were created using existing photolithographic methods to make a pattern of microfeatures on silicon wafers. First, the silicon wafers were coated with a negative photoresist. Using an aligner, a mask was positioned on top of a wafer and exposed. The wafers were subsequently developed so as to remove the unexposed photoresist resulting in the desired pattern. The wafers were then etched using deep reactive-ion etching (DRIE) and the remaining photoresist subsequently removed. As seen in Figure 3.3, the microposts were cylindrical structures nominally 12-16 μm tall, a pitch of 16.5 μm, and a cavity fraction F_c of about 87%. The microribs were rectangular structures nominally 12-16 μm tall, a pitch of 32 μm, and a cavity fraction F_c of about

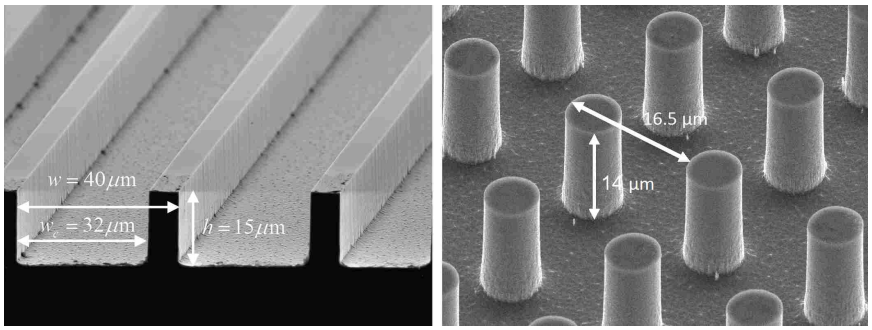

Figure 3.3: SEM images of the microscale rib (left) and post (right) surface topographies as designed and created with common photolithography techniques on silicon wafers.

80%. The variation in height was a result of the edges of the wafer being etched deeper than the center. This didn't affect the experiments since the water stayed largely in the Cassie-Baxter state and thus the liquid only touched the tops of the microfeatures. In order to allow good adhesion of a hydrophobic coating, the surfaces were coated with a thin chromium layer (100 nm) using a thermal evaporator. These surfaces were then coated with a thin layer of Teflon® (<200 nm) which, along with the microstructure, render the surfaces superhydrophobic. The contact angles for the surfaces are shown in Table 3.1. For each surface there is a static (θ_s), advancing (θ_a), and receding (θ_r) contact angle, and for the rib surface there is a set of contact angles for the longitudinal (in the direction of the ribs) and transverse (perpendicular to the direction of the ribs).

Table 3.1: Static, advancing, and receding contact angles for smooth hydrophilic, post SH, and rib SH surfaces

Surface	$\theta_s(^\circ)$ Long/Trans	$\theta_a(^\circ)$ Long/Trans	$\theta_r(^\circ)$ Long/Trans
Smooth	69	87	49
Post	165	168	140
Rib	140/149	150/168	140/133

3.3.2 Experimental Setup

The setup, shown in Figure 3.4, consisted of a wafer holder with sides raised above the wafer in order to hold the amount of water required to create the liquid film. The height of the water above the wafer surface was determined by first touching a needle, which was connected to a micrometer, to the top of the surface. The needle was then moved to contact the top of the film surface and the difference gave the film thickness h. Due to the high contact angle of the SH surfaces, the film thickness was constrained to be at least 5 mm to prevent it from pulling off the surface. This thickness was known with a 2% uncertainty and was used for all experiments. The value for $\delta = h/d$ varied due to changes in droplet diameter, d, from 1.014-1.035. This range of δ was within the range previously stated to have a weak influence on the crown dimensions and can be considered nominally the same.

Above the surface, a syringe was fixed in place to a stand which was varied in height between experiments. The syringe was filled with water and the piston was manually pressed to eject the water through the nozzle. The water built up at the end of the syringe until the weight of the droplet caused it to detach and fall. The same nozzle was used for all experiments and had a diameter of 1.2 mm. The resulting droplet diameters, d, ranged from 4.83 to 4.93 mm with an uncertainty of 0.5-2%. Each surface was tested at four drop heights, resulting in four impingement velocities, V, from 2.26-4.30 m/s measured within 1%. Experiments were performed over a Weber number ($We = \rho V^2 d/\sigma$) range of about 340 to 1230 having an uncertainty of 2-3% (See Appendix A.2). Deionized water was used for all experiments, and the density, ρ, and surface tension, σ, were both held constant at 998.2 kg/m^3 and 0.0728 N/m respectively.

The sides of the wafer holder were made of thin transparent acrylic which allows for viewing horizontally over the wafer both above and below the liquid film surface. A high speed camera was positioned parallel to the wafer as shown in Figure 3.4. Figure 3.5 shows a sample of cropped images in sequential order where the wafer surface is at the very bottom of the image and the free surface of the film is the dark line above the wafer.

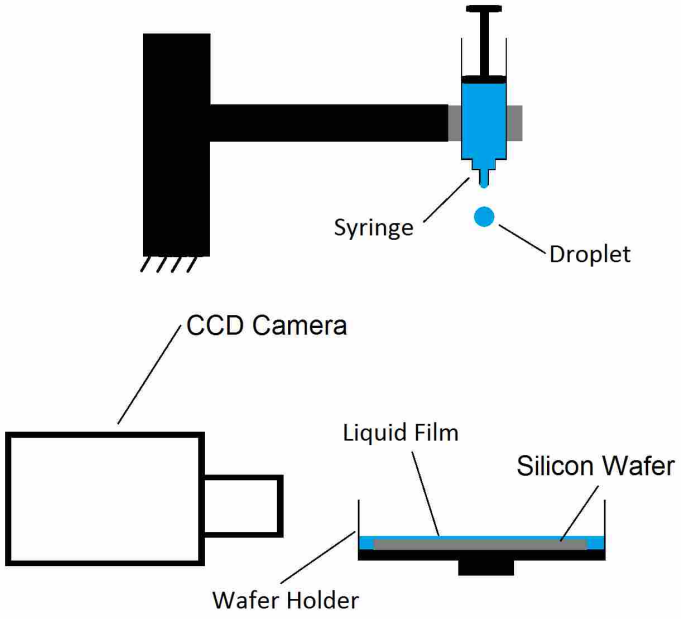

Figure 3.4: Schematic of the apparatus used to perform droplet impingement experiments.

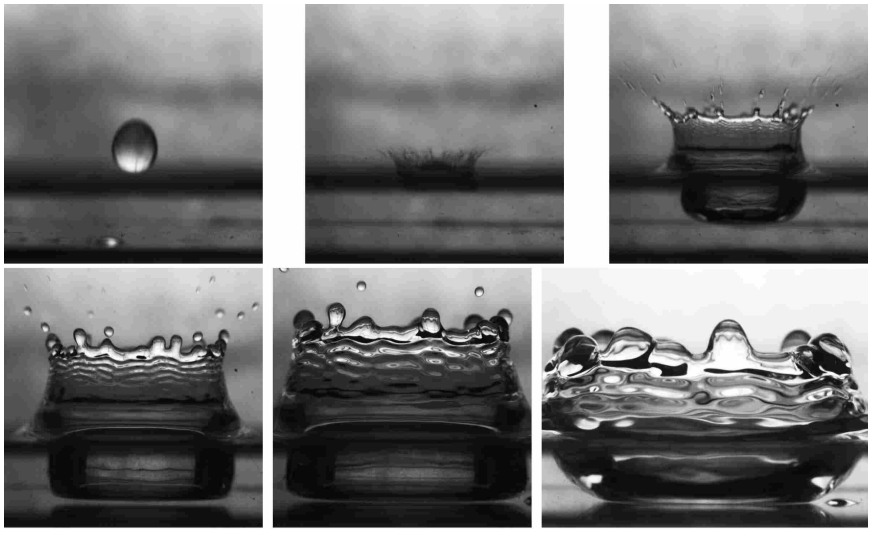

Figure 3.5: Images displaying a sequence of events covering the droplet initial impact, crown formation, and crown dissipation.

All length measurments were made by finding the pixel distance in the obtained images and then applying a calibration. Using the frames just before impingement, V was measured by finding the distance traveled between frames and multiplying by the frame rate. The crown height, H, was determined by finding the average height from the top surface of the film to the top rim of the crown. This is demonstrated in Figure 3.6 along with the crown height measurement which Cossali et al. [1] utilized. Since Cossali et al. measured to the bottom rim, it is clear that their

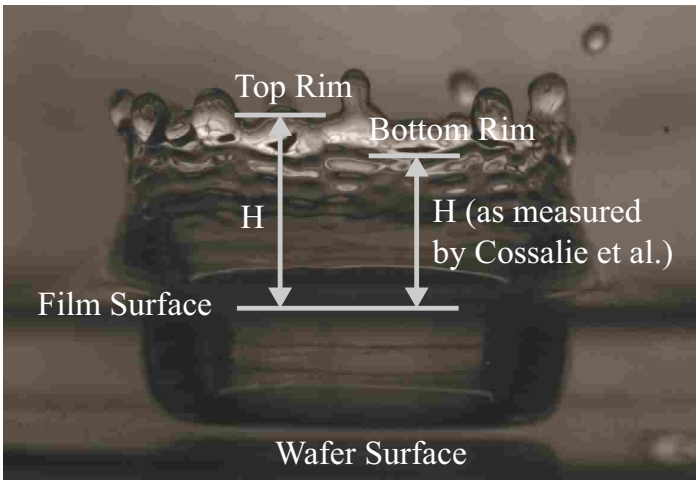

Figure 3.6: A sample image demonstrating the crown height measurement, H, spanning from the liquid surface to the top rim. As a comparison to the method of Cossali et al. [1], the crown height measurement from the liquid surface to the bottom rim is also denoted.

data will underestimate the maximum height of the liquid in the crown. Determination of the magnitude of the maximum height could be performed fairly accurately by taking the maximum value. However, the time at which the maximum height occurred lacked precision due to the error being greater than the slope near this point. In order to accurately obtain both the value and the time at which the maximum was achieved, a 3rd order polynomial fit was applied to the data surrounding the expected maximum height. Figure 3.7 shows a data set from the smooth surface and We of 340 with a corresponding curve fit having an R-squared value of 0.98. The frame at which the maximum occurred was then used to find the corresponding crown diameter, D. Measurements from the images were all made with an uncertainty of ± 4 pixels which was about ± 0.156 mm. The nondimensional ratios H/d and D/d were both calculated with a total uncertainty of 2-13%. Only one case exceeded 7.5%, reaching 13%, which occurred for the rib longitudinal H/d at $We = 340$. It was clear that one sample did not display any jetting in the crown rim and obtained a much lower maximum height. It is possible that a transition region between jetting and no jetting of the crown exists near this We, though no other test had such a contrast in the crown dynamics.

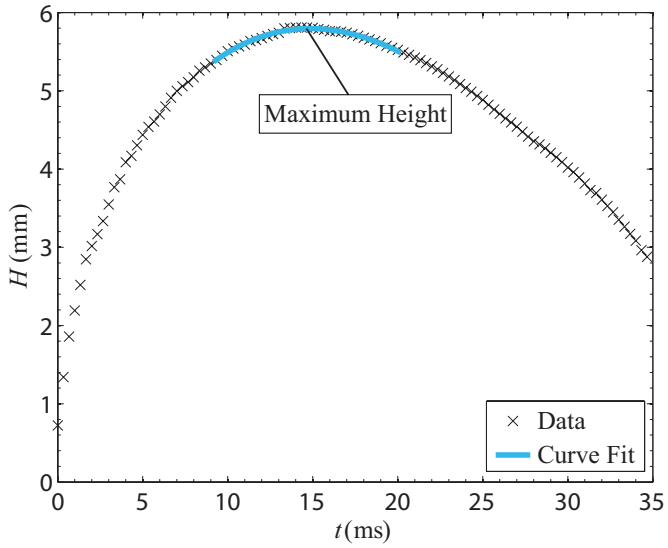

Figure 3.7: Crown height, H, as a function of time, t, for the smooth surface with a We of 340. A 3rd order polynomial fit of the data surrounding the maximum is shown to demonstrate how the maximum height and time of occurrence were estimated.

Three different surfaces were used, a smooth hydrophilic surface, a post SH surface, and a rib SH surface. The rib surface was tested at two different orientations, parallel to the camera plane (longitudinal) and perpendicular (transverse). Experiments were replicated fives times for each set of conditions.

3.4 Results

Images of the crown near maximum height, for each surface at $We = 1230$, are shown in Figure 3.8. The shape of the crown remains consistent for all surfaces, with a thin liquid wall extending vertically upward and culminating in a crown rim. In Figure 3.8 the each crown rim is wavy, has protruding jets, and splashing droplets can be seen above. Each of these is caused by surface tension, as it causes any curvature in the rim to increase as the crown spreads. The amount of jetting and splashing appears constant regardless of surface type. This consistency between surfaces proved true at each *We* tested, even though as *We* decreased there was a decrease in the amount of jetting and splashing.

(a) (b) (c) (d)

Figure 3.8: Images of the crown near maximum height and at $We = 1230$ are shown for (a) longitudinal direction rib SH, (b) transverse direction rib SH, (c) post SH, and (d) smooth hydrophilic surfaces.

It was observed during the collapse of the crown that air bubbles were often entrained at the wafer surface and could affect subsequent impinging droplets. This was most severe for SH surfaces. Figure 3.9 shows a sequence of images demonstrating thin film retraction caused by a droplet impinging at the location of an entrained bubble on a SH surface. The images are all from a top-down view with the droplet appearing in the first image as a white sphere, due to reflective

particles which were added to qualitatively assess the phenomenon. Several bubbles are shown scattered across the surface. After the droplet impinges and the thin film formed, the bubbles become holes in the film which then pull off the surface due to the high contact angle. The entire wafer surface within the crown is exposed as the crown begins to collapse. Though no change in the crown dynamics was observed due to thin film retraction, when this phenomenon was observed the results were not used.

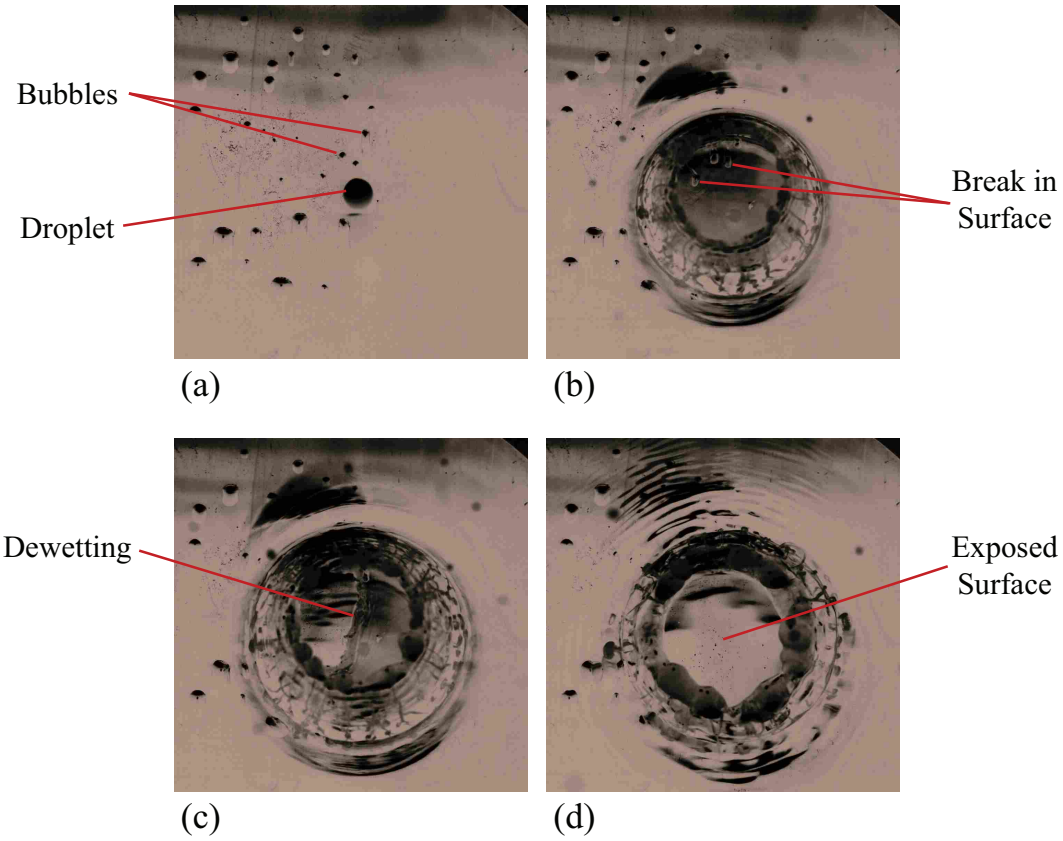

Figure 3.9: Top view images of a droplet impinging a SH surface (a) before impingement, (b) bubbles creating holes in thin film, (c) retraction of the thin film, and (d) complete retraction of thin film with wafer surface exposed.

First the crown height evolution through time in Figure 3.10 is explored. Shown here is the ratio of crown height to droplet diameter, H/d, as a function of the nondimensional time parameter $\tau = V_0 t/d$. Data sets from the longitudinal direction of the rib SH surface are plotted for *We* of 340 (solid circles) and 950 (open triangle). Also plotted is a data set from Cossali et al. on a hydrophilic surface for *We* of 843 and δ of 1.13 (crosses). Direct comparison is difficult

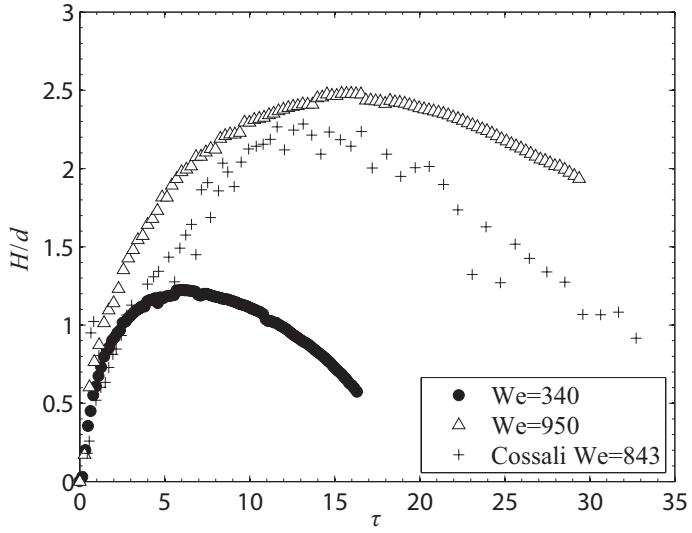

Figure 3.10: Ratio of crown height to droplet diameter, H/d, as a function of nondimensional time, τ, for the rib surface in the longitudinal direction for *We* values of 340 and 950. A data set at *We* of 843 obtained by Cossali et al. [1] is plotted for comparison.

as Cossali et al. measured the crown height as the bottom of the crown rim, instead of the top. Even so, the data of Cossali et al. lies below 950, as expected due to the lower *We* and lower measuring location. Additionally, it lies above the data for *We* 340 due to the much higher *We*, and noting the measurement location may lower it, but not below this *We*. Qualitatively, the curves all follow the same sharp initial increase to a maximum, and then a decrease at a reduced slope. The variation is fairly smooth throughout, and locally abrupt changes are due to the uncertainty in the measurements. As *We* increases, the height and time of maximum height both increase. Because *We* varied due to the droplet momentum, we conclude that the increase in height is due to the increased momentum being transfered into the crown. The increase in momentum also increases the amount of time before the crown is decelerated to zero velocity (at maximum height).

Figure 3.11 shows the ratio of crown height to droplet diameter, H/d, as a function of *We* for each surface. Each data point is the average of the 5 tests performed for the given surface and *We*. The *We* ranges from 340-1230, and as *We* increases there is an increase in H/d of 1.5-2. In general, the height increases linearly with *We* as the increase in droplet momentum results in an increase in the redirected vertical velocity within the crown. There is a slight decrease from linearity at high *We*, especially for the post surface. It is possible that it is approaching limits on

the height due to increased splashing. Droplets lost due to splashing both decreases the crown height by removing material and by decreasing the momentum of the crown.

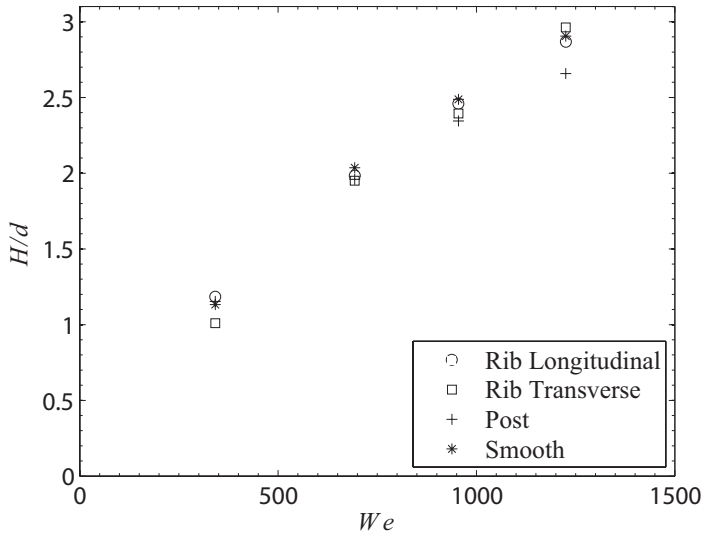

Figure 3.11: Ratio of maximum crown height to droplet diameter, H/d, as a function of We for rib SH (both longitudinal and transverse), post SH, and smooth hydrophilic surfaces.

Comparing the nondimensional maximum crown height, H/d, for each case there is no significant difference between the surfaces. This is indicative of the lack of importance of surface structure since the liquid film was several orders of magnitude larger than the surface features and even on the same order of magnitude as the droplet. These criterion place the flow in the regime of weak surface effects [1]. For large We the crown on the post surface is slightly lower, and for the largest We the difference is just beyond the uncertainty. It is possible that the water/air interface between the posts could not be supported for high impact velocities. If so, the cavities would be flooded around the point of impingement, causing the surface to act like a rough surface. This would alter crown dynamics, such as an increase in splashing, however, this could not be confirmed from observation.

Figure 3.12 shows the ratio of crown diameter at maximum height to droplet diameter, D/d, for each surface. Each point corresponds to the same We given in Figure 3.11. The range of D/d is from just over 3 to just over 5 which is an increase of as much as 56%. This increase is due to greater droplet momentum and the increase in time for the crown to reach a maximum

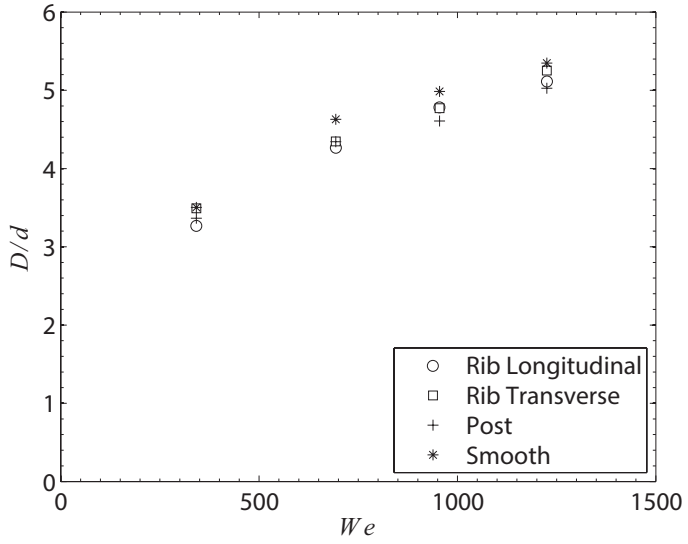

Figure 3.12: Ratio of crown diameter at the maximum crown height to droplet diameter, D/d, as a function of *We* for rib SH (both longitudinal and transverse), post SH, and smooth hydrophilic surfaces.

height. With greater momentum transfered to the crown, the spreading velocity is increased. A larger spreading time combined with the larger velocity increases D/d. While the increase is linear, there is some curvature suggesting limiting factors at high *We*. In this case, it is not expected that splashing is the cause since the momentum of splashing droplets is largely vertical. Instead, it is likely due to viscous effects. This behavior is supported by Trujillo and Lee [29] who developed a numerical model which demonstrated that as *Re* (or *We*) increases, it approaches the inviscid case, and by lowering *Re*, the relative effect of viscous losses increases. The data is again largely indistinguishable between surfaces. The smooth surface maintains greater values, but for the most part stays within the uncertainty of the other surfaces.

3.5 Conclusions

We have explored a droplet impinging on a SH surface covered with a liquid film and compared the crown dynamics to that of a smooth hydrophilic surface. This furthers droplet impingement on liquid film research as no characterization of this phenomenon has been made utilizing SH surfaces previous to these experiments. Because of the high contact angle and decreased wetted area characteristic of SH surfaces, it was expected that the crown behavior would be altered.

However, due to the relatively large (5 mm) film thickness required to maintain a film on the SH surfaces, the effect of the surface is largely negated and any difference there may be is lost in the intrinsic variation of the experiments. The only confirmed difference occurred due to bubble entrainment on the SH surfaces which cause the thin film within the crown to pull off the surface. A much larger *We* is required for a film of this thickness if any significant difference is to be seen. If the droplet size is increased the surface effects may be better observed, but the droplet dynamics may be more difficult to maintain. The droplets used in this study were nominally 4.9 mm in diameter, which is greater than many applications thus far. If a thinner film could be maintained on the SH surfaces then more useful results could be obtained. We note the impossibility of this (for a flat surface) and thus a problem of greater interest may be multiple droplet interactions on a surface, ie a train of droplets.

CHAPTER 4. DROPLET TRAIN IMPINGEMENT ON SUPERHYDROPHOBIC SURFACES

4.1 Abstract

An investigation into the dynamics of droplet train impingement onto superhydrophobic (SH) surfaces was made. The surfaces were patterned with either post or rib microfeatures. The height of the features for both was nominally 15 μm and the spacing for the post and ribbed surfaces were 16.5 μm and 32 μm respectively. Droplet frequencies ranged from 600-4600 Hz with sizes varying from 0.7 to 1.5 mm in diameter. When each individual droplet impinged on the surface, a crown formed which spread out radially until reaching a semi-stable or regularly oscillating breakup diameter. At this point the water would break up into droplets or filaments continuing radially outward. In some cases the crown would breakup before reaching the breakup diameter, causing splashing. A comparison to previous experiments on hydrophilic surfaces shows a distinct difference in splashing at low frequency. The breakup diameter was measured over a Weber number range of 72-2800. The data was collapsed as a function of a combination of the Reynolds number (Re), Capillary number (Ca), and Strouhal number (St), resulting in $Re^{0.7}CaSt$. The SH surface exhibiting rib microfeatures, displayed an elongated breakup due to the anisotropic surface features. When compared to the post SH surface, this resulted in a breakup diameter which was increased in the direction longitudinal to the ribs and reduced in the direction transverse to the ribs. The breakup diameter for the droplet train was compared to, and shown to be greater than, the breakup diameter which has been shown to occur with a jet impinging on a SH surface.

4.2 Introduction

4.2.1 Superhydrophobicity

Fluid dynamics involving superhydrophobic (SH) surfaces has been of great interest in recent research. This is due to the manner in which these surfaces alter the fluid flow compared to smooth hydrophilic and even hydrophobic surfaces. SH surfaces are characterized by their high contact angle, $\theta > 120°$, as shown in Figure 4.1. This material property is ideal in situations requiring reduced liquid/surface contact area. In order to achieve such high contact angles, a hydrophobic coating must be applied to a microstructured surface if it is not natively hydrophobic. The microstructure enhances the hydrophobicity of the surface when the fluid sits above the air cavities between the microstructure (Cassie-Baxter state). If the pressure exceeds the Laplace pressure, defined as $\Delta P = \sigma(1/R_1 + 1/R_2)$, where σ is the surface tension and R_1 and R_2 are the radii of curvature of the meniscus, then the fluid penetrates the cavities. When the surface wets in this fashion, it is termed the Wenzel state and the contact angle is lower [5].

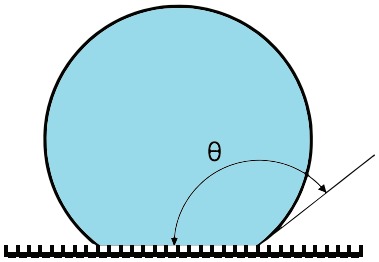

Figure 4.1: Drawing of a droplet of water sitting on a SH surface. The contact angle, θ, is the angle from the surface in contact with the water to the liquid surface extending outward.

The lotus leaf is often referred to as a prime example of a SH surface, where the leaves use hydrophobic waxes covering a micro-topography of papillae [3]. There are various approaches to duplicate this phenomenon. Etching silicon or growing carbon nanotubes are common methods developed to generate micro, or nano, structures [4]. These methods can be utilized to create random or carefully patterned microstructures such as posts or ribs. Other methods, such as using abrasives or a spray-on coating, will only allow for randomized microstructures. Natively hydrophilic

surfaces (surfaces with $\theta < 90°$) are often coated with a hydrophobic coating (such as wax or Teflon®) to render them SH. These surfaces have been shown to decrease condensation buildup on condensers by allowing water to roll or even jump off surfaces [14]. When in the Cassie-Baxter state, SH surfaces display an apparent slip velocity near the surface due to negligible shear at the water-air interface over the cavities [7–9]. The slip is a function of the distance between adjacent microstructures (pitch) and the fraction of water in contact with air (cavity fraction). An increase in either of these surface properties results in an increase in the slip [10]. This decreases the friction drag, which is desirable in microchannels and microfluidic devices where viscous effects from the wall require large pressure gradients to drive the flow [11].

4.2.2 Droplet Impingement

The dynamics of a single droplet impinging on a hydrophilic surface are dominated by inertial, viscous, and surface tension forces. The impingement process is characterized by the spreading of the droplet and rebounding capillary waves while the bulk of the droplet volume is stationary on the surface where impingement occurred. At high impact velocities, peripheral splashing can occur as well [22]. If a droplet impinges on a hydrophobic or SH surface, the droplet retracts and can lift off the surface [23]. In the SH scenario where a micro or nano-structure is present, at the location of droplet impact the stagnation pressure may exceed the Laplace pressure, forcing fluid into the normally air filled cavities and pinning the droplet to the surface [24]. For large impact velocities, perturbations in the droplet symmetry cause fingering, or a non-uniform droplet perimeter. At even higher impact velocities the fingering protrusions break off, resulting in peripheral splashing. For SH surfaces, this splashing occurs at lower impact velocities than hydrophilic surfaces. Also, the droplet has been shown to experience differing shear stresses dependent on the surface microfeatures [25].

When a droplet impacts a hydrophilic surface completely wetted by a liquid film, a remarkably different process ensues. This type of impingement is important in spraying applications, such as cooling or painting operations, as well as with falling rain. In these processes, a film of liquid is left behind by previous droplets. Spreading and splashing still occur, but a crown is formed at the leading edge and the thin film promotes increased splashing at the top of the crown, going upward. Cossali et al. [1] subdivided the process into four separate phases: droplet impact, crown

formation, jet formation and break-up, and crown collapse (see Figure 4.2). A crown is formed at the leading edge of the spreading droplet and propagates outward while the crown height grows and then dissipates. The film eventually collapses inward and results in liquid jetting upward. If the momentum within the crown is sufficient, breakup of the crown, or splashing, occurs. Droplets produced by splashing separate from the top of the crown and have a significant vertical velocity component.

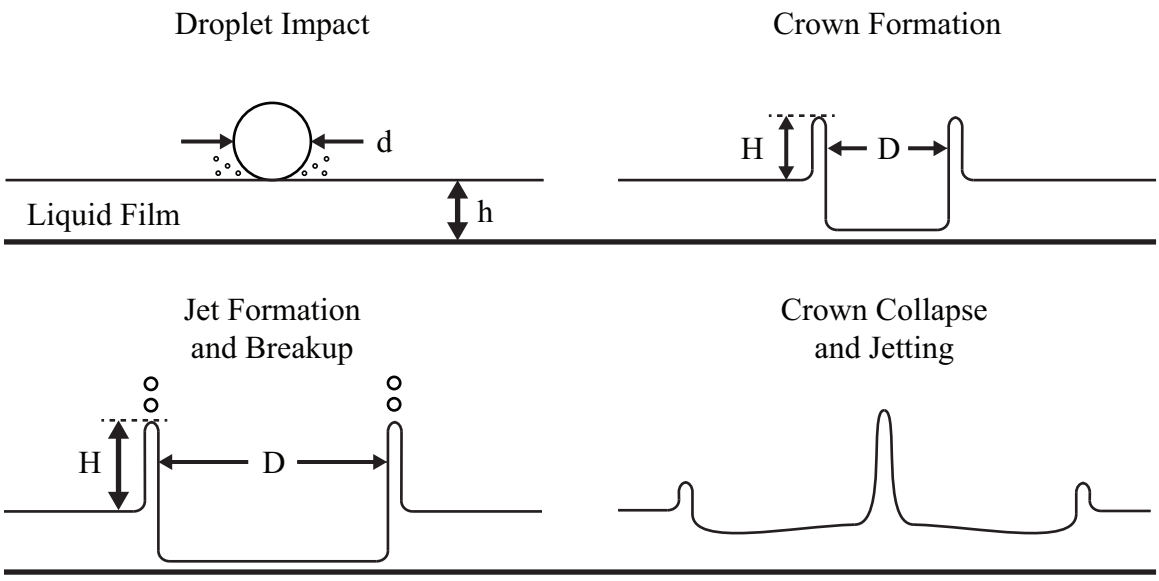

Figure 4.2: Diagram showing the temporal progression of a droplet impinging on a surface covered with a liquid film.

Vander Wal et al. [26] investigated the effect of film thickness on the impingement dynamics by using the film thickness to droplet diameter ratio, $\delta = h/d$, to give two regimes. The first regime, $0.1 \leq \delta \leq 1$, exhibited two modes of splashing, prompt and delayed. The prompt splashing, which occurs immediately after impact with the film, has little effect on the impingement process due to the low amount of mass ejected. Delayed splashing is caused by instabilities in the rim of the crown causing jetting and breakup. The second regime, $1 \leq \delta \leq 10$, was characterized by reduction in the prompt splashing and inhibited delayed splashing which resulted in an overall decrease in splashing. Alternatively, Cossali et al. [27] suggested two regimes based on a comparison with the surface roughness, R_a. A thin liquid film was described as $h \gg R_a$, where the

surface had a weak influence. A very thin film was then for $h \approx R_a$, where the surface had a strong influence. The primary effect of increased surface roughness was an increase in splashing.

A droplet train is a series of fluid droplets which move in sequence along the same trajectory. In practice, droplets will not usually be uniform in size, trajectory, or frequency of impact. Spray cooling, for instance, will have many fluid droplets impinging randomly across a surface, which has been shown by Sivakumar [30] to give differing results than a uniform droplet train. However, an investigation into the characterization of the impingement process can be made, and in the case of certain printing applications, these droplet trains do accurately describe the process as the ink droplets are guided precisely to certain locations in order to gain high resolution.

In a droplet train, each droplet hits the surface following the general dynamics of a single droplet hitting a surface with a thin film of the same fluid. If the frequency of impinging droplets is low, then the crown collapses before each subsequent impingement and remains as if it were a single droplet. By increasing the frequency, subsequent droplets will impinge before the crown collapses as shown in Figure 4.3. In this case, each droplet impinges on the thin film created by the previous droplet. When this occurs on a hydrophilic surface, a quasi-steady crater is maintained by the periodic outward momentum of each crown. [31].

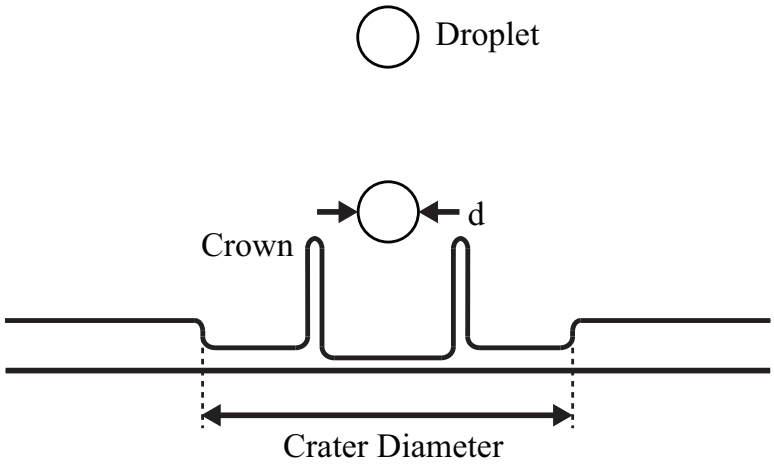

Figure 4.3: Diagram showing a droplet train impinging on a surface.

Since breakup within the crown rim is not affected by the previous or subsequent crowns, splashing dynamics are usually considered the same as for a single droplet impinging a thin film. Thus the relations described previously are used for both. There is a potential difference due to the

presence of the crater in droplet train impingement which was not accounted for in previous work. Yarin and Weiss, for example, used a curved surface to keep any liquid from building up [28]. While no study has done so for a droplet train, jet impingement with an imposed film thickness has shown that the hydraulic jump, or crater, will decrease as the film thickness increases [20, 21]. If this occurred for a droplet train, it might interfere with the splashing dynamics.

A combination of a droplet train model and experiments were performed by Yarin and Weiss [28]. They predicted the onset of splashing using the following equation:

$$\varepsilon = (\alpha \nu^{1/2} f^{2/3})/(\rho V_0^4) \tag{4.1}$$

Here, α is the surface tension, ν the kinematic viscosity, f the droplet frequency, ρ the fluid density, and V_0 the droplet impact velocity. It was determined that splashing occurs when ε is less than a nominal value of 18^{-4}. Yarin and Weiss also experimentally determined the splashing threshold for a range of frequencies and impact velocities. Doing so, they found a correlation for the splashing threshold as $Ca = C\lambda^{3/4}$, where $Ca = (\mu V)/\sigma$ is the Capillary number, $\lambda = (\nu/f)^{1/2}\sigma/(\rho\nu)^2$, and C is a constant with a weak dependence on surface roughness. For a given λ, splashing in the crown occurred for values of Ca above the splashing threshold, and values below resulted in deposition (no splashing). As λ increased, the value of Ca required to cause splashing decreased.

4.2.3 Jet Impingement

The droplet train impingement shown in Figure 4.3 closely resembles jet impingement on a hydrophilic surface. While jet impingement does not involve any crown dynamics, a hydraulic jump does occur [16, 17], and is similar to the crater formed by droplet impingement. Thus, a review of jet impingement on a SH surface becomes useful in understanding and comparing to droplet impingement on a SH surface. When a jet impinges a SH surface, the thin film region breaks up into droplets instead of forming a hydraulic jump [20, 21]. Figure 4.4 shows jet impingement and thin film breakup on a SH surface. The fluid momentum for a thin slice of the spreading film is defined as $M = \int \rho V^2 dA$, where ρ is the density, V is the velocity profile across the thickness of the film, and A is the cross-sectional area (spanning the circumferential length and

film thickness). The high contact angle results in a significant surface tension force, F_S, pulling inward. This causes the thin film on the surface to break up into droplets due to surface tension forces at a critical location denoted as the breakup radius, R_B. At this point M balances with F_S. It was shown that as the jet Weber number, $We_j = \rho V^2 d_j/\sigma$, based on the jet diameter, d_j, increased, the breakup radius increased due to the greater momentum in the thin film allowing it to spread further before surface tension caused breakup [13, 20, 21].

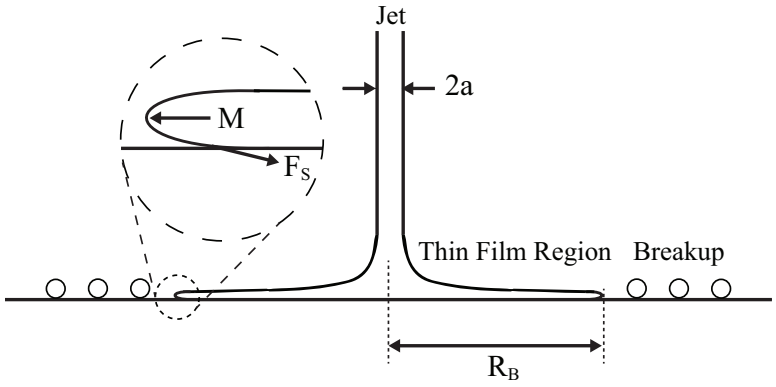

Figure 4.4: Diagram showing breakup of thin film due to a laminar jet impinging on a SH surface.

The dynamics of droplet impingement onto a hydrophilic surface covered by a thin film have been explored, and experiments have been performed using various surface features. Recently there is an increasing desire to utilize SH surfaces in environments, such as spray cooling operations, where surfaces are subjected to droplet impingement. While droplet train impingement experiments have been performed on hydrophilic surfaces, impingement on a SH surface normal to the droplet train has not. The dynamics of a droplet train impinging a SH surface are explored here to compare splashing dynamics to previous work along with identifying the unique features introduced by the structure of the SH surface. Also, it is expected that breakup will be similar to the thin film breakup due to jet impingement on a SH surface. This breakup is analyzed here with comparisons to varying surface features and to jet impingement.

4.3 Methods

In order to perform the experiments, SH surfaces with a patterned microstructure were produced in-house. Also, a setup was designed and built in order to produce a droplet train which would impinge on a SH surface. The setup included a method for measuring the breakup diameter for comparison between surfaces and to jet impingement.

4.3.1 Surface Fabrication

The SH surfaces were created using existing photolithographic methods to make a pattern of microfeatures on silicon wafers. First, the silicon wafers were coated with photoresist, then, using a mask, exposed and developed so as to remove the photoresist in the desired pattern. The wafers were then etched and the photoresist subsequently removed. Micropost and microrib patterned surfaces were used for all experiments. As seen in Figure 4.5, the microposts were cylindrical structures nominally 12-16 μm tall, a pitch of 16.5 μm, and a cavity fraction F_c of about 87%. The microribs were rectangular structures nominally 12-16 μm tall, a pitch of 32 μm, and a cavity fraction F_c of about 80%. The variation in height was a result of the edges being etched deeper than the center. This didn't affect the experiments since the water stayed largely in the Cassie-Baxter state and thus the liquid only touched the tops of the microfeatures. In order to allow good adhesion of a hydrophobic coating, the surfaces were coated with a thin chromium layer (100 nm) using a thermal evaporator. These surfaces were then coated with a thin layer of Teflon® ($<$200 nm) which, along with the microstructure, render the surfaces superhydrophobic. The contact angles for the surfaces are shown in Table 4.1. For each surface there is a static (θ_s), advancing (θ_a), and receding (θ_r) contact angle, and for the rib surface there is a set of contact angles for the longitudinal (in the direction of the ribs) and transverse (perpendicular to the direction of the ribs).

Table 4.1: Static, advancing, and receding contact angles for smooth hydrophilic, post SH, and rib SH surfaces

Surface	θ_s(°) Long/Trans	θ_a(°) Long/Trans	θ_r(°) Long/Trans
Post	165	168	140
Rib	140/149	150/168	140/133

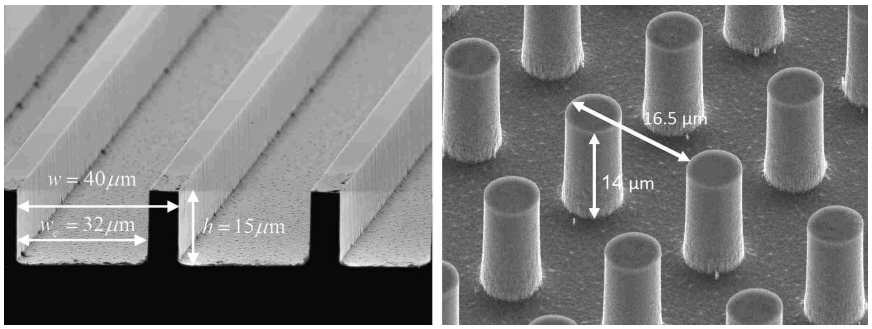

Figure 4.5: SEM images of the microscale rib (left) and post (right) surface topographies as designed and created with common photolithography techniques on silicon wafers.

4.3.2 Test Setup

A setup similar to that used by Yarin and Weiss [28] was used to create continuous droplet trains. As shown in Figure 4.6, water was pressurized in a tank and connected via a valve to a glass tube. The tube was rigidly secured horizontally at its base and, at the other end, in firm contact with a piezoelectric transducer which was also held rigidly in place. At the location of the transducer, the tubing was curved 90 degrees such that the tip, which acted as the nozzle, was vertical. Different nozzle sizes were utilized to obtain jet diameters, d_j, ranging from 0.56-0.73 mm. As the water exits, perturbations were induced into the jet from the vibration of the transducer. These regular perturbations caused the jet to break up into a regularly dispersed stream of droplets or a droplet train. The droplets continued to flow vertically downward until they impinged on the wafer below the nozzle. The setup allowed for control and measurement of flow speeds. In the right panel of Figure 4.6, a side view, taken using a high speed camera, of a droplet train is shown. This setup was able to create uniformly-sized and equally-spaced droplet trains at small scales of order 100-1000 μm which is comparable to previously created droplet generators [28, 32, 33].

The flow rate, Q, was measured via a collection method with a range of 0.42-1.82 mL/s and an uncertainty of less than 2.22%. The droplet train frequency, f, was initially measured using high speed video, but it was determined to be the same as the transducer input frequency. The frequency range was 600-4600 Hz, and the output of the signal generator supplying the transducer had an uncertainty of 0.01%. By assuming the generated droplets were spheres uniform in size and spacing, a conservation of mass approach can be used to obtain the droplet diameter. This is done by equating the measured flow rate to the volume of a single droplet multiplied by the frequency.

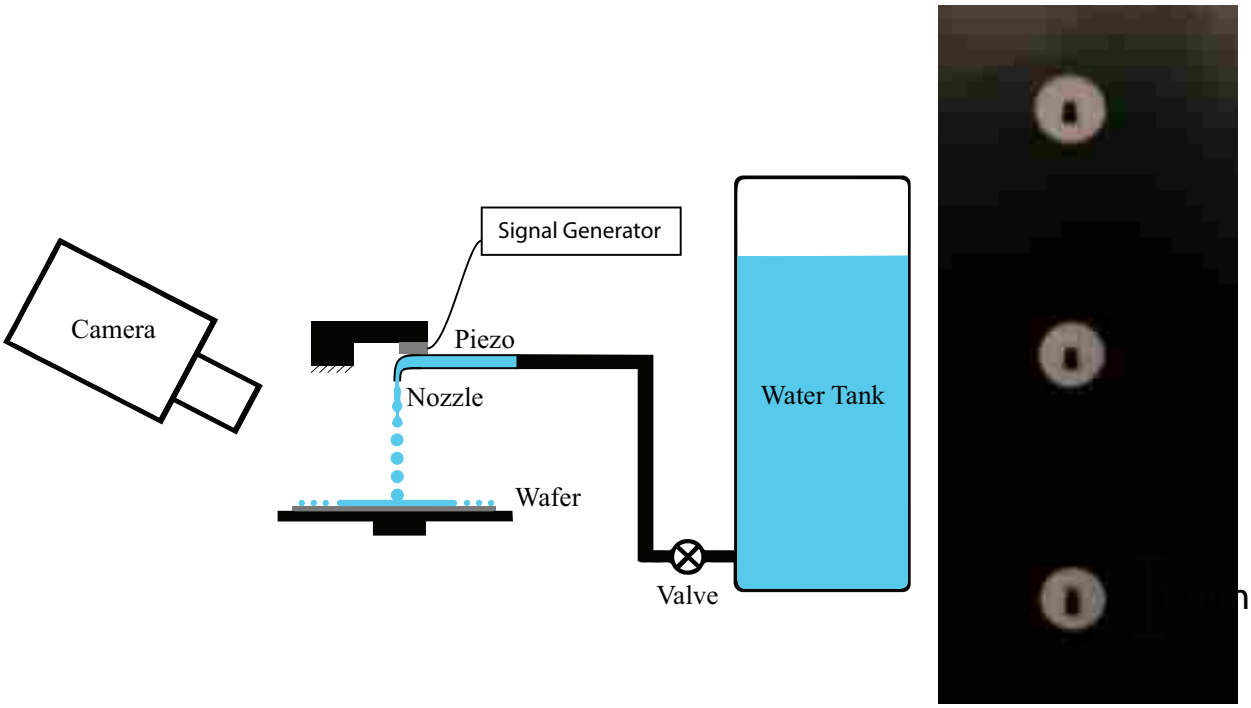

Figure 4.6: Setup of experimental apparatus (Left) and a high speed image of droplets produced (Right).

Since the volume of a single droplet depends only on the diameter, then the droplet diameter can be solved using the relation $d = 2(3Q/4\pi f)^{1/3}$. With the added assumption of negligible acceleration due to gravity, the exiting velocity of the jet, $V_j = 4Q/\pi d_j^2$, can be used for the droplet velocity. This method of determining droplet diameter and impingement velocity matched well with a sample of direct measurements and resulted in ranges of 0.7-1.5 mm and 2.3-10.3 m/s. The Weber number, $We = (\rho V^2 d)/\sigma$, and Reynolds number, $Re = (\rho V d)/\mu$, ranged from 72-2800 and 2.3×10^3-16.8×10^3 respectively. The uncertainty for both remained less than 5% (See Appendix A for uncertainty analysis). The Capillary number, $Ca = (\mu V)/\sigma$, ranged from 0.03-0.23 and had an uncertainty of 1-6% with larger uncertainties at lower flow rates due to reduced relative accuracy in volumetric measurements. The Strouhal number, $St = fd/V$, ranged from 0.18-0.83 with an uncertainty of 1-1.7%. A high speed camera was placed at an angle of 45-60°relative to the plane of the surface. For the case of the rib surface, the direction parallel to the ribs (the longitudinal direction) was oriented horizontally in the camera plane, and the direction perpendicular to the ribs (the transverse direction) was vertical in the image. High speed video was recorded at 3000 frames per second (fps), however, the number of images in which data was gathered was lower

at an effective 600 fps. Horizontal measurements, and vertical for the rib surface, of the breakup diameter (d_B) were averaged over these frames for each test. The uncertainty for the breakup diameter ranged from 1-10%, but 94% of the data, all at the higher end of values, was less than 5%.

Splashing was not quantified by the number or size of produced droplets, but splashing was determined qualitatively for several of the experiments on the post surface. The viscosity length, $\lambda = (\nu/f)^{1/2}\sigma/(\rho\nu)^2$, was calculated for these tests in order to determine splashing regimes.

4.4 Results

4.4.1 General Observations

Displayed in Figure 4.7 is a schematic and an image from testing of a droplet train impinging a SH surface. Both prompt and delayed splashing were observed as defined by Vander Wal et al. [26]. Also, a crown forms at the point of impingement and propagates outward as would happen with a hydrophilic surface. Instead of forming a crater, as it would with a hydrophilic surface, the high contact angle causes the thin film to break up similar to jet impingement on a SH surface. As with a jet, a balance of the surface tension and momentum exists at the location of breakup.

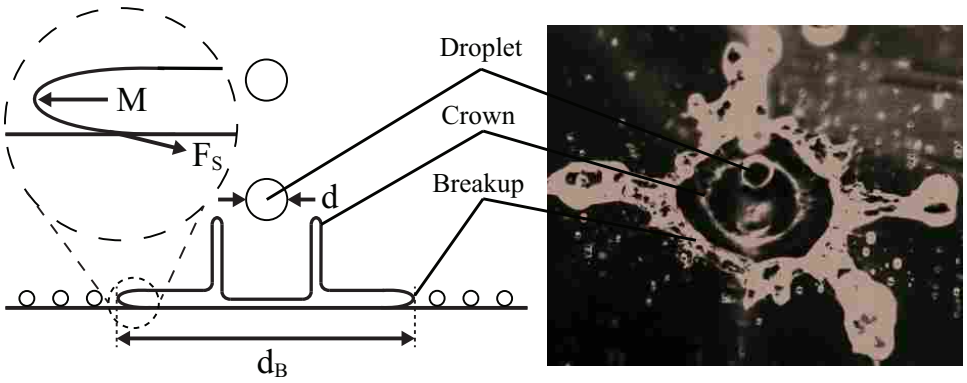

Figure 4.7: Schematic and image of a droplet train impinging a SH surface.

At the point of impingement, a dark region was observed as shown in Figure 4.8 for experiments on both the post and rib surfaces. This dark region was caused by water from the impinging

droplets penetrating the microstructure, causing localized wetting of the surface. Wetting was observed to occur in every experiment, though lighting conditions sometimes masked it in high speed video. The wetted region was consistently larger than the size of the droplet, but less than the breakup diameter. There was no change in this region over the course of an experiment except when retraction caused dewetting by decreasing the breakup diameter into the wetted area.

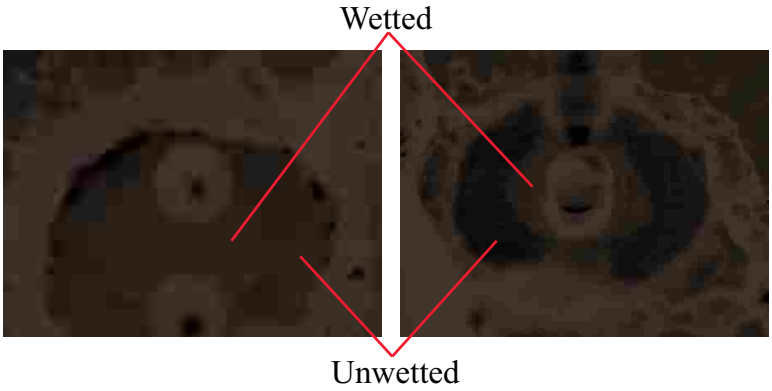

Figure 4.8: Regions of wetting are shown for droplet train impingement on both a post (Left) and rib (Right) microstructured SH surface.

In some instances the droplet train apparatus produced noticeably deformed droplets. While in general these did not have a significant effect on the impingement, some extreme cases altered the shape of the breakup diameter. The droplets in these cases had large oscillations as they moved toward the surface, and were severely elongated at the point of impingement. The result is shown in Figure 4.9, where these deformed droplets are impinging on a post SH surface. The breakup is elliptical in shape, instead of circular, even though the surface features are isotropic. A characteristic of this anomaly was a complete redirection of the flow towards each end of the elongated portion of the breakup. As the liquid propagates outward, it lifts off the surface in a jet which then curves back down due to gravity. It was determined that the direction of elongation in breakup could be controlled by the direction of the elongation in the droplets at impingement. Further analysis of this phenomenon was not made, and these cases of large droplet deformation were neglected in subsequent data analysis.

4.4.2 Splashing

Splashing was observed qualitatively and used in Figure 4.10 to plot Ca as a function of λ where the squares represent splashing at the crown rim and the filled circles represent deposition (no splashing). A comparison of the splashing and deposition regimes is made to that of Yarin and

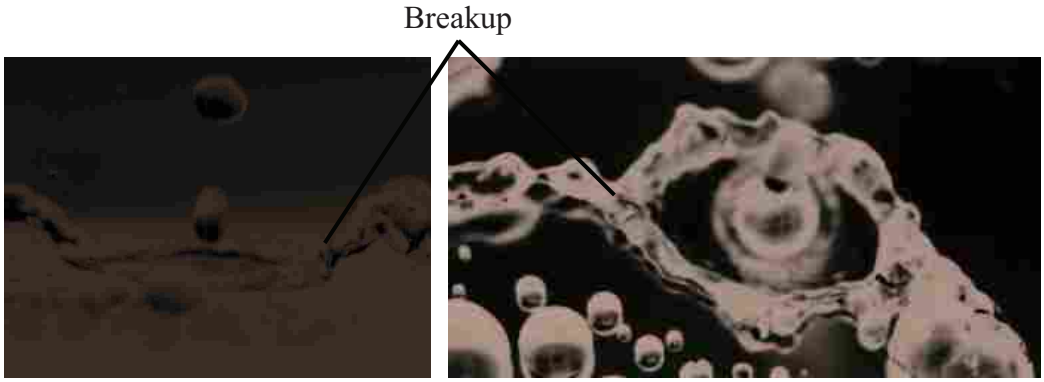

Figure 4.9: Side (a) and top (b) views of elongated breakup caused by large deformation of impinging droplets on a SH post surface.

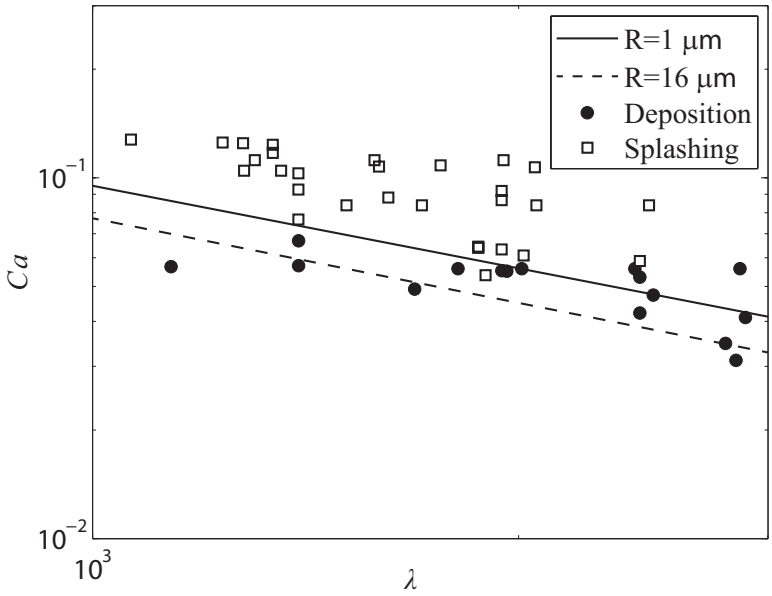

Figure 4.10: Ca as a function of the viscosity length, λ. Correlations are shown for hydrophilic surfaces having roughness, R_a, of 1 and 16. Data for post SH surfaces is shown for splashing (open squares) and deposition (closed circles)

Weiss [28]. The solid and dashed lines are the splashing threshold for surface roughness values (the average feature height) of R_a =1 and 16 μm, respectively, as determined by Yarin and Weiss through a fit of their data for droplet train impingement experiments performed on hydrophilic surfaces. For Ca or λ values greater than the threshold, splashing occurs, and for lower values, deposition occurs. The data for post SH surfaces is displayed as open squares, indicating the presence of splashing, and solid circles, for deposition. Since much of the microstructure was wetted at the point of impingement, the effective roughness of the surface can be estimated as that of the microstructures, which is around R_a of 6 to 8 μm.

While there is insufficient data to determine the threshold accurately, the transition from splashing to deposition is near the correlation for R_a =1. There is an exception to this at large values of λ. In this region, deposition occurred for Ca values well above the correlation where splashing was expected to occur. By observation of the impingement at these points, there is a significant amount of fluctuation in the breakup diameter. These fluctuations are caused by the high λ, or low frequency, which allows time for partial retraction between sequential droplets. The retraction results in both a thicker film and increased buildup at the edge of breakup, which can both decrease splashing. Because the retraction decreases the breakup diameter, the crown may reach the breakup diameter before delayed splashing has occurred. Reduced splashing due to retraction and buildup mimics what would occur if a crater formed due to droplet train impingement on a hydrophilic surface. However, the experiments by Yarin and Weiss were performed on slightly curved surfaces to remove any crater or buildup. It's likely that if Yarin and Weiss used a flat surface and had a crater, the discrepancy would be reduced by the retracting crater decreasing splashing. Overall, there is a weak influence of λ on the splashing transition over the range of experiments, and because λ varies as $1/\sqrt{f}$, a large change in frequency is required to alter the splashing threshold.

4.4.3 Breakup Diameter Data

The measured ratio of breakup diameter to droplet diameter, d_B/d, is plotted in Figure 4.11 as a function of Re (a) and the combined Capillary and Strouhal numbers $CaSt = fd\mu/\sigma$ (b). Multiplying Ca by St simply replaces the V term with the product fd, and creates a modified Capillary number which still compares viscous and surface tension forces. Note the different

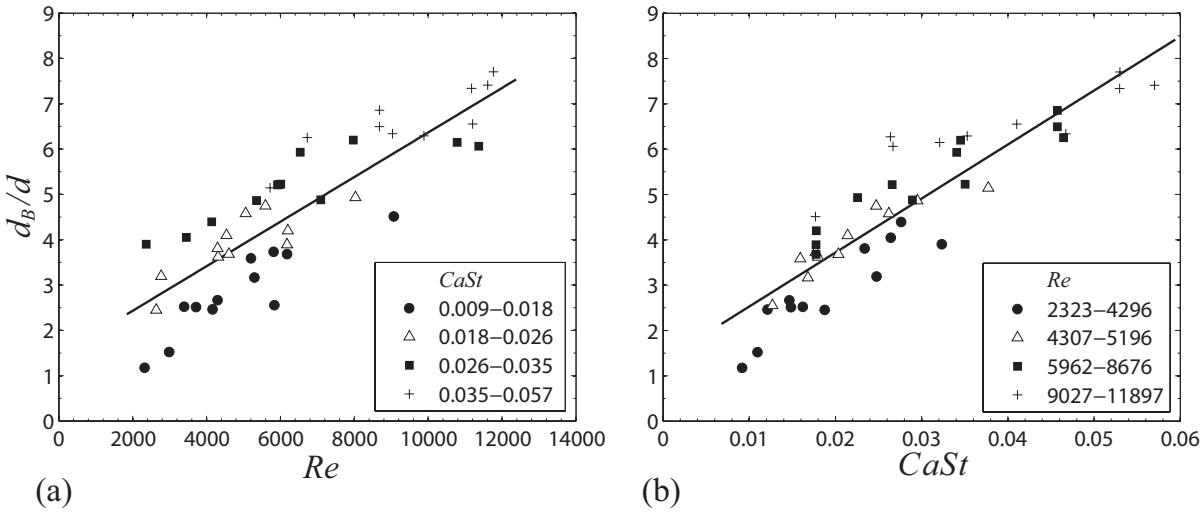

Figure 4.11: Ratio of breakup diameter to droplet diameter, d_B/d, as a function of (a) *Re* and (b) *CaSt*. A linear fit of the data is plotted with R-squared values of 0.73 and 0.81 for (a) and (b) respectively. The data in (a) and (b) are separated into ranges of *CaSt* and *Re* respectively.

shapes which correspond to different ranges of *CaSt* and *Re* in (a) and (b) respectively. The data is for experiments performed on the post SH surface. In both (a) and (b), an increase in *Re* and *CaSt* generally resulted in an increase in d_B/d as shown by the fit line. In (a), low *CaSt* ranges, which generally have a low *Re*, fall below the fit line. Similarly, higher ranges of *CaSt* are above. The same trend is displayed in (b) for the given ranges of *Re*. Within these experiments a change in *Re* was due to a change in the momentum of a single droplet, and thus the general increase in d_B/d can be attributed to the increase in momentum. Similarly, *CaSt* increased due to an increase in the average mass flow rate, which also is attributed to the general increase in d_B/d. In each plot is a linear trend of the data having R-squared values of 0.73 and 0.81 for (a) and (b) respectively. Individually, neither parameter achieves a collapse of the data. However, restricting *CaSt*, in (a), and *Re*, in (b), to a specific range does reduce the scatter of the data. Thus, a collapse may be achieved by utilizing both parameters.

Using a combination of the nondimensional numbers in the form $Re^a(CaSt)^b$, the data collapsed best for $a = 0.7$ and $b = 1$ as shown in Figure 4.12, resulting in $Re^{0.7}CaSt = \rho^{0.7}V^{0.7}d^{1.7}f/(\mu\sigma)$. This term is a ratio comparing the droplet momentum and average flow rate to the viscosity and surface tension of the liquid. Since the fluid properties of the water were kept constant, the only variation in this term is due to V, d, and f. Changing these values equates to a change in the overall

momentum of the droplets impinging on the surface. Figure 4.12 gives a plot of d_B/d as a function of this momentum term, $Re^{0.7}CaSt$, along with threshold values for splashing and retraction. The general trend is an increase in d_B/d and a decrease in the slope for an increase in the momentum term. No upper limit was observed throughout the experiments, and values immediately above are expected to follow the same trends. An exponential fit of the data, as shown in Figure 4.12, follows the form $d_B/d = C_1 e^{k_1(Re^{0.7}CaSt)} + C_2 e^{k_2(Re^{0.7}CaSt)}$, where the coefficients and R-squared value are given in Table 4.2.

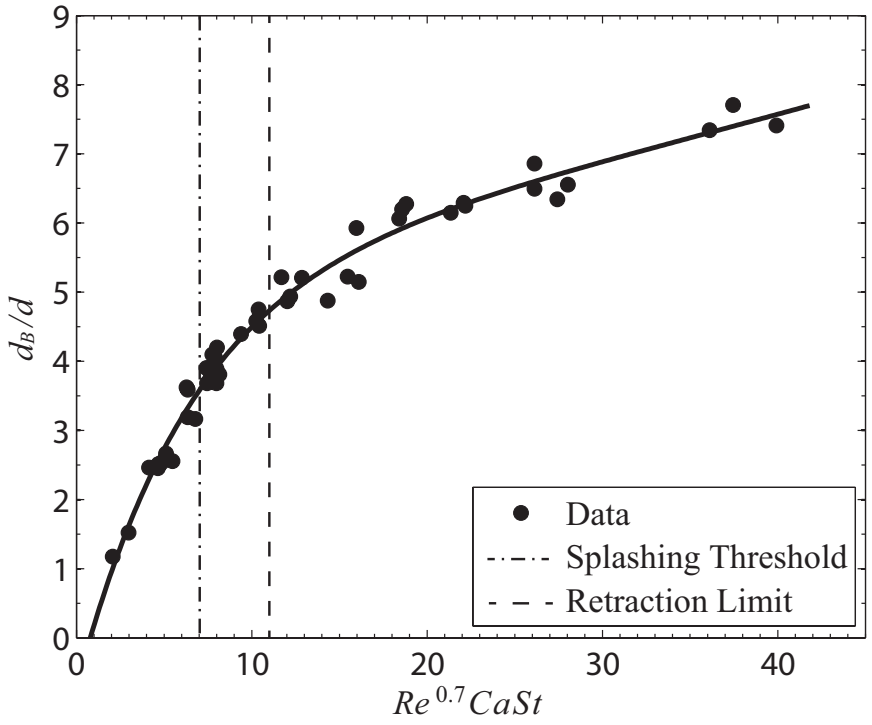

Figure 4.12: Ratio of breakup diameter to droplet diameter, d_B/d. Also plotted are the threshold values for splashing and retraction and an exponential fit of the data.

Table 4.2: Coefficients of the exponential fit with corresponding R-squared value are given for the post SH surface.

Surface	**Coefficients**				R^2
	C_1	k_1	C_2	k_2	
Post	5.399	8.450×10^{-3}	-6.123	-0.1491	0.98

Low values of $Re^{0.7}CaSt$ are characterized by deposition, or no splashing in the crown, and retraction of the breakup diameter. High values are characterized by splashing and little or no retraction. The transition to splashing occurs around $Re^{0.7}CaSt$=7, and larger values generally equate to greater splashing. Retraction is present below $Re^{0.7}CaSt$ values of nominally 11. In this region, the outward propagating crowns collided with the retracting breakup diameter, decreasing the average breakup diameter. Retraction also reduced momentum at the breakup diameter, as it induced an inward velocity which had to be overcome by each crown propagating outward. The decrease in momentum caused increased buildup at the breakup diameter. It is noted that as the buildup increases it will begin to exert a non negligible hydrostatic force. It was estimated analytically that if the buildup reached a thickness of 2 mm, the hydrostatic force would be the same order of magnitude as the surface tension. The lowest data points around $Re^{0.7}CaSt$ of 2-3 approached this condition with buildup nearing as much as 1 mm. Below $Re^{0.7}CaSt$=2, the breakup diameter retracts completely and the thin film region vanishes before a subsequent droplet impinges. The dynamics then change to a single droplet impinging a relatively thick pool.

The sharp slope at low $Re^{0.7}CaSt$ is due to the decrease in the magnitude of retraction as $Re^{0.7}CaSt$ increases which results in much larger breakup diameters. When the retraction becomes small and it cannot be decreased sufficiently to make a difference, a lower slope prevails. The decrease in slope at high $Re^{0.7}CaSt$ can also be attributed to the onset of splashing, which reduces the momentum within the crown as less liquid reaches the breakup diameter.

In order to better analyze the effect of frequency and momentum independently, the previously described exponential fit was utilized to produce the surface plot in Figure 4.13 of d_B/d_j as a function of f and $We_j = \rho V^2 d_j/\sigma$. Here the volume flow rate and impingement velocity of the droplets are used to obtain a corresponding jet. This is done by equating the volume flow rate of the droplet train to that of a jet, and results in

$$3/4\pi d^3 f = \pi d_j^2 V \tag{4.2}$$

where the droplet train is represented by the left hand side and the jet on the right. Equation 4.2 is solved for the jet diameter, d_j

$$d_j = \sqrt{\frac{3d^3 f}{4V}} \tag{4.3}$$

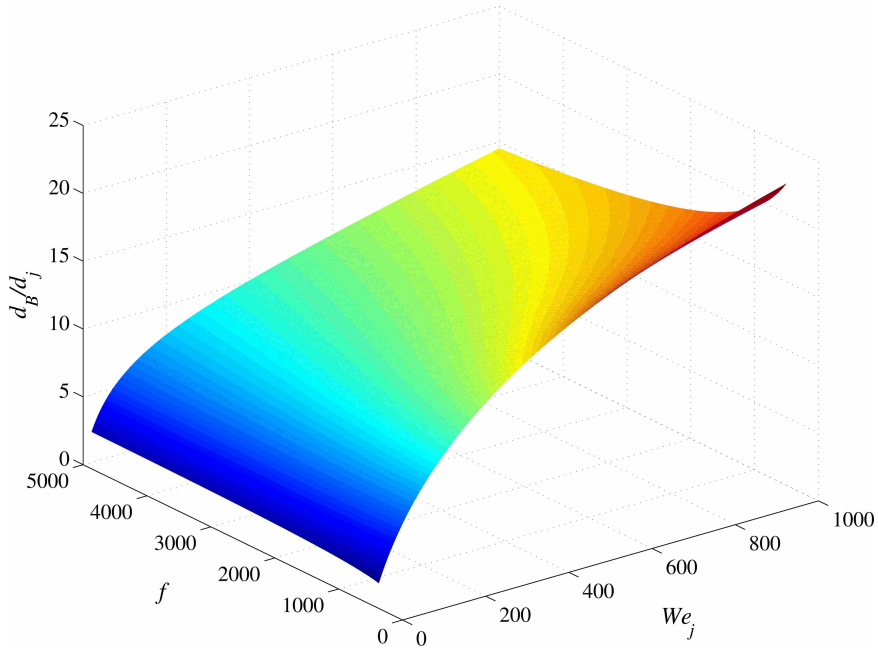

Figure 4.13: Plot of d_B/d_j as a function of f and We_j determined using an exponential fit of the data shown in Figure 4.12.

For negligible acceleration due to gravity, the diameter of such a jet is the same as the initial jet diameter from the experiments. In Figure 4.13, d_j and the fluid properties are constant. As We_j increases, d_B/d_j increases due to greater momentum, while the slope decreases. The effect of varying f is noticeably less than it is for We_j. Also, increasing f decreases d_B/d_j at high We_j. This is because droplet size is reduced which increases d_B/d_j. At low We_j there is a slight increase in d_B/d_j as f increases because the effect of retraction overcomes that of droplet size.

A comparison of the breakup diameter for a droplet train to a liquid jet is shown in Figure 4.14. In the plot the ratio of breakup diameter over jet diameter (d_B/d_j) for the post SH surface, utilizing just one nozzle size and, therefore, a single jet diameter ($d_j = 0.624$ mm), is plotted as a function of We_j. Data points are separated into three frequency ranges with 400-1000 Hz as circles, 1000-2050 as triangles, and 2050-5000 as squares. The dashed lines are obtained from the correlation used to produce Figure 4.13 at each of the frequency bounds which the data is sorted into. An analytical model for jet impingement breakup by Prince [13] is plotted as a solid line. For all data points, the breakup location for the droplet train remains below and within about 30% of the jet impingement model. Because the main difference between droplet train and jet impingement is the crown, it follows that the crown dynamics cause the reduction in breakup diameter. In

the formation of the crown, radial momentum is reduced by the vertical redirection of part of the flow into the crown. Also, as We_j is decreased, retraction increases and reduces breakup diameter, while at We_j well above the splashing threshold, there is momentum lost in splashing before the crown reaches the breakup diameter. From the lines determined using the correlation, at low f it is possible for droplet train breakup diameters to exceed that of the jet. For f of 500 Hz and We_j ranging from nominally 300 to 1000 the combination of retraction and splashing is minimized, which maximizes the breakup diameter of the droplet train compared to the jet.

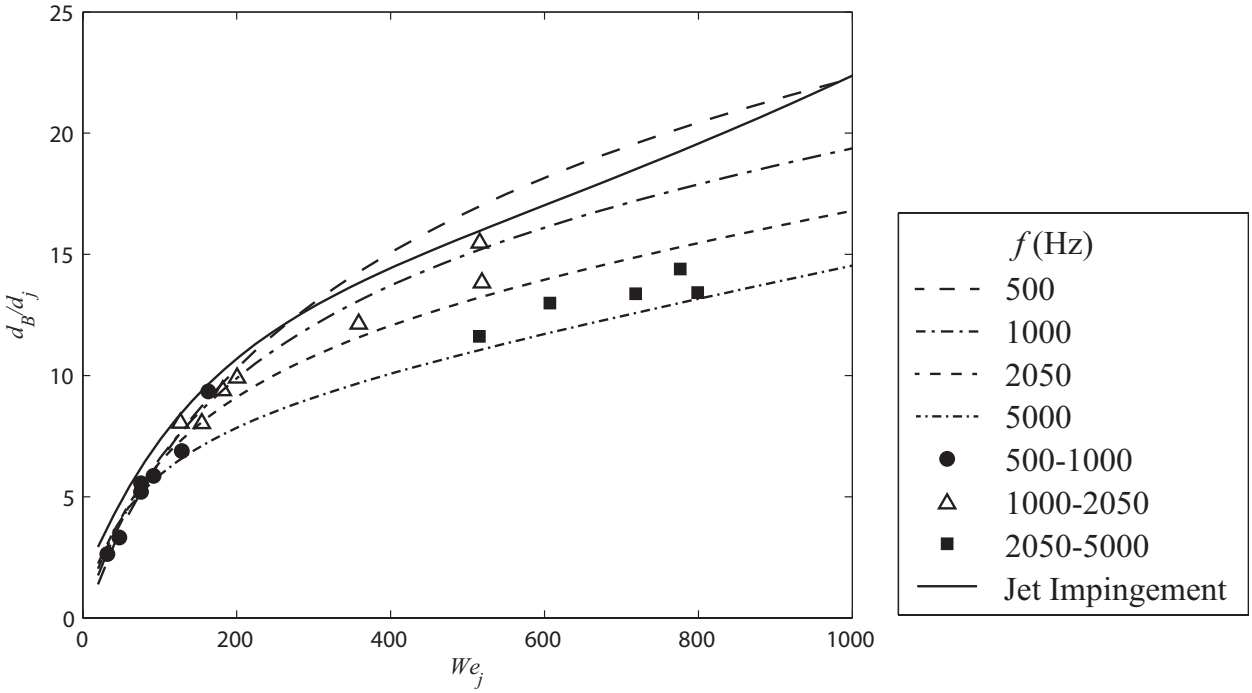

Figure 4.14: Comparison of breakup diameters for droplet train impingement with jet impingement. The ratio of breakup diameter to jet diameter, for both a droplet train and a jet are plotted as functions of Re_j. Lines are obtained from the correlation of the post data at frequencies of 500, 1000, 2050, and 5000 Hz.

For large We_j, at least above 100, increasing f decreases d_B/d_j. While higher frequency would seem to approach the continuous flow of a jet, the subsequent reduction in droplet size, with flow rate constant, instead reduces the breakup diameter. For low We_j this same effect will not hold true since increasing f at a low We_j results in a decrease in retraction, which would increase the breakup diameter.

In Figure 4.15, data obtained using a rib SH surface is compared to the post SH surface reproduced from Figure 4.12. Since the rib structure is anisotropic, the breakup diameter is shown for both the longitudinal and transverse directions denoted by triangles and squares respectively. An exponential fit of the form $d_B/d = C_1 e^{k_1(Re^{0.7}CaSt)} + C_2 e^{k_2(Re^{0.7}CaSt)}$ is also plotted for each data set. Table 4.3 gives the values of these coefficients along with the R-squared value for the fit. The same lower limit and trends are the same as for the post SH surface. It should be noted that surface plots similar to Figure 4.13 can be obtained for the rib SH surface. The d_B/d values for the longitudinal are generally greater (average of 12%) than that of the post surface, and the transverse is below (average of 8%). It is noted that the increase in the longitudinal direction exceeds that of the decrease in the transverse direction. This could be due to the effect of slightly different cavity fractions and contact angles, or because the post surface isn't truly isotropic. At low $Re^{0.7}CaSt$ the data all converges as the difference between directions has a much smaller diameter over which to exert influence. Another difference from the post SH surface is the point at which retraction ceases. In the longitudinal direction this transition occurs at a higher value, near $Re^{0.7}CaSt = 12$, while in the transverse direction it occurs at a lower value, near $Re^{0.7}CaSt = 9$. This can be attributed to the increase and decrease in time required for the crown to reach the breakup diameter in the longitudinal and transverse directions respectively.

Table 4.3: Coefficients of the exponential fit with corresponding R-squared value are given for the rib SH surface in the longitudinal and transverse directions.

Surface	**Coefficients**				R^2
	C_1	k_1	C_2	k_2	
Longitudinal	5.840	9.678×10^{-3}	-7.375	-0.1656	0.92
Transverse	4.795	9.583×10^{-3}	-4.854	-0.1408	0.88

As with the case of jet impingement on a rib SH surface, the flow in the thin film region is being redirected along the longitudinal direction (see Section 4.2.3). This turning of the flow can be a result of two separate phenomena. In the Cassie-Baxter state the flow would be turned by a greater slip in the longitudinal direction. If the fluid is in the Wenzel state, the fluid would be turned into the longitudinal direction by the physical barrier the ribs form in the transverse direction. Since partial wetting of the microstructure occurs, it is a combination of these two

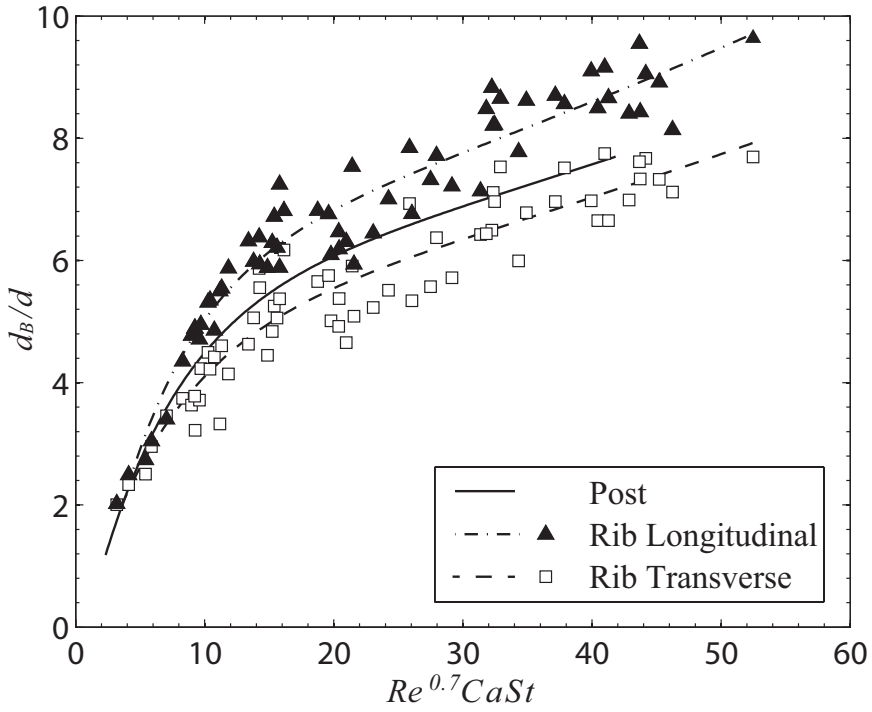

Figure 4.15: Ratio of breakup diameter to droplet diameter, d_B/d

processes which turns the flow. The relative magnitude of turning is likely related to the percent of area in which wetting occurs. The main differences the droplet train has from a jet is a reduced elongation. The longitudinal direction had breakup diameter about 20% larger than the transverse direction for the droplet train compared to about 40% for a jet [21].

4.5 Conclusions

This work contributes to droplet train impingement research by characterizing the dynamics using superhydrophobic (SH) surfaces patterned with either post or rib microfeatures. We found that the dynamics are similar to a hydrophilic surface in that a crown is formed due to each droplet impingement, which spreads out radially until reaching a semi-stable or regularly oscillating crater radius. Dynamics differ in that at this point the water either breaks up into droplets or filaments while continuing radially outward. The regime of splashing was similar to previous experiments on hydrophilic surfaces with the exception of high λ (low f) where deposition occurred for much higher Ca. The breakup diameter was measured over a range of We of 72-2800 and collapsed best as a function of $Re^{0.7}CaSt$. Both the post and the rib SH surface displayed an increase in d_B/d for

increasing $Re^{0.7}CaSt$ along with a decrease in the slope. Compared to jet impingement on a SH surface, a droplet train has a consistently smaller breakup diameter for large frequencies, and is caused by lost momentum within the crown. At low frequencies, increased droplet size increases the droplet train breakup diameter and can exceed the jet breakup diameter. Also, above We_j of nominally 100, increasing frequency causes the droplet breakup diameter to be even smaller, while below We_j a decrease in frequency produces the same result. These effects are likely due to smaller droplet sizes at higher frequencies and high We_j reducing the breakup diameter, while retraction is increased at lower frequencies and low We_j. The breakup diameter for the rib SH surface was found to be elongated in the longitudinal direction of the ribs while reduced in the transverse direction. This increase was microstructure turning the flow such that momentum increased in the longitudinal direction.

CHAPTER 5. CONCLUSIONS

The proposed use of superhydrophobic surfaces as self-cleaning surfaces [12] and in heat transfer processes [14] has made further investigation into the impingement dynamics of great interest. The combination of a hydrophobic coating and microfeatures has been demonstrated previously to produce large contact angles [3] which can cause liquid breakup [20, 21] and slip [7, 9–11]. Here we have performed experiments to further previous work on liquid impingement on superhydrophobic surfaces.

Research in the area of liquid impingement on SH surfaces has focused primarily on jet and single droplet impingement. Jet impingement in particular has been explored for submerged and free SH surfaces. However, we explore a transition regime between these two cases, which involves both thin film breakup and a hydraulic jump. Other holes which this research attempts to fill are in the area of droplet impingement on a SH surface. One is the case of a liquid film present on the surface and another is multiple droplets impinging in a continuous stream. By characterizing these impingement processes, a more complete view of liquid interaction with SH surfaces is achieved.

5.1 Jet Impingement

The dynamics of fluid flow over a SH surface due to jet impingement have been explored over a specific transition region between the well known thin film breakup and a classical hydraulic jump. Due to changes in downstream depth, a region where both phenomenon occur is found. Experiments involving three different *Re* numbers from 1.9-2.2$\times 10^4$ were performed to track the free hydraulic jump as it collapsed. The transition occurred over a range of downstream depths, H/a, of nominally 1. For a given downstream depth during the transition, the free hydraulic jump radius is greater for larger *Re*. Also, as *Re* increases, the radius at which the free hydraulic jump reaches the breakup radius increases. A transition was not observed for *Re* below the minimum

tested value 1.9×10^4, but is expected to occur for values above the maximum tested *Re* of 2.2×10^4.

5.2 Droplet Impingement on Liquid Coated Superhydrophobic Surface

The crown dynamics of a droplet impinging on a SH surface covered with a liquid film was compared to that of a smooth hydrophilic surface. Because of the high contact angle and decreased wetted area characteristic of SH surfaces, it was expected that the crown behavior would be altered. However, due to the relatively large (5 mm) film thickness required to maintain a film on the SH surfaces, the effect of the surface is largely negated and any difference there may be is lost in the intrinsic variation of the experiments. The only confirmed difference occurred due to bubble entrainment on the SH surfaces which cause the thin film within the crown to pull off the surface. A much larger *We* is required for a film of this thickness if any significant difference is to be seen. If the droplet size is increased the surface effects may be better observed, but the droplet dynamics may be more difficult to maintain. The droplets used in this study were nominally 4.9 mm in diameter, which is greater than many applications thus far. If a thinner film could be maintained on the SH surfaces then more useful results could be obtained, though we note the impossibility of this (for a flat surface).

5.3 Droplet Train Impingement

The dynamics of droplet train impingement on superhydrophobic (SH) surfaces patterned with either post or rib microfeatures are similar to a hydrophilic surface in that a crown is formed due to each droplet impingement which spreads out radially until reaching a semi-stable or regularly oscillating crater radius. Dynamics differ in that at this point the water either breaks up into droplets or filaments while continuing radially outward. The regime of splashing was similar to previous experiments on hydrophilic surfaces with the exception of high λ (low f) where deposition occurred for much higher *Ca*. The breakup diameter was measured over a range of *We* of 72-2800 and collapsed best as a function of $Re^{0.7}CaSt$. Both the post and the rib SH surface displayed an increase in d_B/d for increasing $Re^{0.7}CaSt$ along with a decrease in the slope. Compared to jet impingement on a SH surface, a droplet train has a consistently smaller breakup diameter

for large frequencies, and is caused by lost momentum within the crown. At low frequencies, increased droplet size increases the droplet train breakup diameter and can exceed the jet breakup diameter. Also, above We_j of nominally 100, increasing frequency causes the droplet breakup diameter to be even smaller, while below We_j a decrease in frequency produces the same result. These effects are likely due to smaller droplet sizes at higher frequencies and high We_j reducing the breakup diameter, while retraction is increased at lower frequencies and low We_j. The breakup diameter for the rib SH surface was found to be elongated in the longitudinal direction of the ribs while reduced in the transverse direction. This increase was microstructure turning the flow such that momentum increased in the longitudinal direction.

REFERENCES

[1] Cossali, G. E., Marengo, M., Coghe, A., and Zhdanov, S., 2004. "The role of time in single drop splash on thin film." *Experiments in Fluids,* **36**(6), pp. 888–900. viii, 8, 9, 28, 29, 33, 37, 38, 43

[2] Marmur, A., 2003. "Wetting on hydrophobic rough surfaces: to be heterogeneous or not to be?." *Langmuir,* **19**(20), pp. 8343–8348. 2

[3] Feng, L., Li, S., Li, Y., Li, H., Zhang, L., Zhai, J., Song, Y., Liu, B., Jiang, L., and Zhu, D., 2002. "Super-hydrophobic surfaces: From natural to artificial." *Advanced Materials,* **14**(24), pp. 1857–1860. 2, 13, 27, 42, 63

[4] Kim, S. H., 2008. "Fabrication of superhydrophobic surfaces." *Journal of Adhesion Science and Technology,* **22**(3-4), pp. 235–250. 2, 13, 27, 42

[5] Murakami, D., Jinnai, H., and Takahara, A., 2014. "Wetting transition from the cassiebaxter state to the wenzel state on textured polymer surfaces." *Langmuir,* **30**(8), pp. 2061–2067. 3, 13, 27, 42

[6] Cassie, A. B. D., and Baxter, S., 1944. "Wettability of porous surfaces." *Trans. Faraday Soc.,* **40**, pp. 546–551. 4

[7] C.-H., C., and C.-J., K., 2006. "Large slip of aqueous liquid flow over a nanoengineered superhydrophobic surface." *Physical Review Letters,* **96**(6), Feb, p. 066001. 4, 13, 27, 43, 63

[8] Davies, J., Maynes, D., Webb, B. W., and Woolford, B., 2006. "Laminar flow in a microchannel with superhydrophobic walls exhibiting transverse ribs." *Physics of Fluids (1994-present),* **18**(8). 4, 13, 27, 43

[9] Maynes, D., Jeffs, K., Woolford, B., and Webb, B. W., 2007. "Laminar flow in a microchannel with hydrophobic surface patterned microribs oriented parallel to the flow direction." *Physics of Fluids (1994-present),* **19**(9). 4, 13, 27, 43, 63

[10] Lee, C., Choi, C.-H., and Kim, C.-J. C., 2008. "Structured surfaces for a giant liquid slip." *Physical Review Letters,* **101**, Aug, p. 064501. 4, 13, 27, 43, 63

[11] Rothstein, J. P., 2010. "Slip on superhydrophobic surfaces." *Annual Review of Fluid Mechanics,* **42**, Jan., pp. 89–109. 4, 14, 27, 43, 63

[12] Bhushan, B., Jung, Y. C., and Koch, K., 2009. "Self-cleaning efficiency of artificial superhydrophobic surfaces." *Langmuir,* **25**(5), pp. 3240–3248. 4, 63

[13] Prince, J. F., 2013. "The influence of superhydrophobicity on laminar jet impingement and turbulent flow in a channel with walls exhibiting riblets." PhD thesis, Brigham Young University. 4, 6, 16, 23, 47, 58

[14] Miljkovic, N., Enright, R., Nam, Y., Lopez, K., Dou, N., Sack, J., and Wang, E. N., 2013. "Jumping-droplet-enhanced condensation on scalable superhydrophobic nanostructured surfaces." *Nano Letters,* **13**(1), pp. 179–187. 4, 13, 27, 43, 63

[15] Cao, L., Jones, A. K., Sikka, V. K., Wu, J., and Gao, D., 2009. "Anti-icing superhydrophobic coatings." *Langmuir,* **25**(21), pp. 12444–12448 PMID: 19799464. 4

[16] E.J., W., 1964. "The radial spread of a liquid jet over a horizontal plane." *Journal of Fluid Mechanics,* **20**, pp. 481–499. 5, 14, 46

[17] Bush, J. W. M., and Aristoff, J. M., 2003. "The influence of surface tension on the circular hydraulic jump." *Journal of Fluid Mechanics,* **489**, aug, pp. 229–238. 5, 14, 46

[18] Prince, J. F., Maynes, D., and Crockett, J., 2012. "Analysis of laminar jet impingement and hydraulic jump on a horizontal surface with slip." *Physics of Fluids,* **24**, p. 102103. 5, 15, 22

[19] Prince, J. F., Maynes, D., and Crockett, J., 2014. "Jet impingement and the hydraulic jump on horizontal surfaces with anisotropic slip." *Physics of Fluids (1994-present),* **26**(4). 5, 6, 15

[20] Johnson, M. G., 2012. "Liquid jet impingement experiments on micro rib and cavity patterned superhydrophobic surfaces in both cassie and wenzel states." Master's thesis, Brigham Young University. 5, 6, 10, 15, 16, 46, 47, 63

[21] Maynes, D., Johnson, M., and Webb, B. W., 2011. "Free-surface liquid jet impingement on rib patterned superhydrophobic surfaces." *Physics of Fluids,* **23**(5), may, p. 052104. 6, 10, 15, 16, 23, 46, 47, 61, 63

[22] Stow, C. D., and Hadfield, M. G., 1981. "An experimental investigation of fluid flow resulting from the impact of a water drop with an unyielding dry surface." *Proceedings of the Royal Society of London. Series A, Mathematical and Physical Sciences (1934-1990),* **373**(1755), pp. 419–441. 7, 28, 43

[23] Bartolo, D., Josserand, C., and Bonn, D., 2005. "Retraction dynamics of aqueous drops upon impact on non-wetting surfaces." *Journal of Fluid Mechanics,* **545**, 12, pp. 329–338. 7, 28, 43

[24] Jung, Y. C., and Bhushan, B., 2008. "Dynamic effects of bouncing water droplets on superhydrophobic surfaces." *Langmuir,* **24**(12), pp. 6262–6269 PMID: 18479153. 7, 28, 43

[25] Pearson, J. T., Maynes, D., and Webb, B. W., 2012. "Droplet impact dynamics for two liquids impinging on anisotropic superhydrophobic surfaces." *Experiments in Fluids,* **53**(3), pp. 603–618. 7, 28, 43

[26] Vander Wal, R. L., Berger, G. M., and Mozes, S. D., 2006. "Droplets splashing upon films of the same fluid of various depths." *Experiments in Fluids,* **40**(1), pp. 33–52. 8, 28, 44, 51

[27] Cossali, G., Coghe, A., and Marengo, M., 1997. "The impact of a single drop on a wetted solid surface." *Experiments in Fluids,* **22**(6), pp. 463–472. 9, 29, 44

[28] Yarin, A. L., and Weiss, D. A., 1995. "Impact of drops on solid surfaces: self-similar capillary waves, and splashing as a new type of kinematic discontinuity." *Journal of Fluid Mechanics,* **283**, pp. 141–173. 9, 10, 29, 46, 49, 54

[29] Trujillo, M. F., and Lee, C. F., 2001. "Modeling crown formation due to the splashing of a droplet." *Physics of Fluids (1994-present),* **13**(9), pp. 2503–2516. 9, 29, 39

[30] Sivakumar, D., and Tropea, C., 2002. "Splashing impact of a spray onto a liquid film." *Physics of Fluids,* **14**(12). 9, 45

[31] Trujillo, M. F., Alvarado, J., Gehring, E., and Soriano, G. S., 2011. "Numerical simulations and experimental characterization of heat transfer from a periodic impingement of droplets." *Journal of Heat Transfer,* **133**(12), October 5, pp. 122201–122201. 9, 45

[32] Lindblad, N. R., 1965. "Production of uniform-sized liquid droplets." *Journal of Scientific Instruments,* **42**(8), pp. 635–638. 49

[33] Verma, R. L., 1989. "A simple source of uniform sized droplets." *Journal of Physics E: Scientific Instruments,* **22**(3), pp. 189–190. 49

APPENDIX A. TABULATED DATA FROM DROPLET TRAIN IMPINGEMENT EXPERIMENTS

Table A.1: Data for droplet train impingement experiments performed on a post SH surface used in Chapter 4.

Post SH Surface Data												
d_j (m)	d (m)	Q (mL/s)	f (Hz)	V (m/s)	Re	We	Ca	St	$Re^{0.7}(CaSt)$	d_B (m)	d_B/d	d_B/d_j
0.000634	0.00119	0.80	670	2.53	2987	104	0.035	0.315	2.96	0.00181	1.52	2.85
0.000634	0.00103	0.72	648	2.27	2323	73	0.031	0.294	2.08	0.00121	1.17	1.90
0.000634	0.00140	0.94	628	2.98	4154	170	0.041	0.295	4.13	0.00345	2.46	5.44
0.000634	0.00125	2.02	2007	6.40	7966	702	0.088	0.392	18.57	0.00774	6.20	12.21
0.000634	0.00126	1.08	848	3.44	4296	203	0.047	0.310	5.12	0.00334	2.66	5.27
0.000634	0.00138	1.22	886	3.85	5286	280	0.053	0.317	6.79	0.00436	3.16	6.88
0.000634	0.00130	1.23	1463	3.90	5056	272	0.054	0.488	10.25	0.00596	4.58	9.39
0.000634	0.00138	2.48	1694	7.87	10779	1167	0.108	0.296	21.34	0.00846	6.15	13.34
0.000634	0.00146	1.35	886	4.27	6196	364	0.059	0.302	8.02	0.00612	4.20	9.65
0.000634	0.00122	0.97	886	3.07	3713	157	0.042	0.351	4.68	0.00305	2.51	4.82
0.000634	0.00114	1.26	1366	4.00	4535	249	0.055	0.389	7.77	0.00467	4.10	7.36
0.000634	0.00120	1.48	1498	4.68	5589	360	0.064	0.384	10.38	0.00569	4.75	8.98
0.000634	0.00129	1.47	1498	4.64	5962	381	0.064	0.416	11.68	0.00673	5.22	10.61
0.000634	0.00129	2.86	3221	9.06	11605	1447	0.125	0.457	39.93	0.00953	7.41	15.03
0.000634	0.00132	2.83	2923	8.96	11760	1451	0.123	0.430	37.46	0.01015	7.70	16.01
0.000634	0.00132	2.69	2923	8.52	11167	1309	0.117	0.452	36.11	0.00966	7.34	15.24
0.000634	0.00119	2.40	2846	7.60	9027	945	0.105	0.446	27.44	0.00756	6.34	11.92
0.000634	0.00144	2.46	2069	7.81	11198	1203	0.107	0.382	28.02	0.00944	6.55	14.89
0.000634	0.00154	2.45	1246	7.77	11897	1272	0.107	0.247	18.79	0.00965	6.27	15.22
0.000634	0.00111	1.63	2472	5.18	5717	407	0.071	0.530	16.10	0.00570	5.14	9.00
0.000634	0.00058	1.30	4069	4.11	2364	134	0.057	0.571	7.43	0.00225	3.90	3.55
0.000352	0.00080	0.66	2689	6.74	5349	496	0.093	0.318	12.01	0.00388	4.86	
0.000352	0.00071	0.47	2689	4.85	3448	230	0.067	0.396	7.91	0.00289	4.05	
0.000352	0.00079	0.73	2689	7.47	5912	608	0.103	0.286	12.85	0.00414	5.21	
0.000352	0.00075	0.54	2689	5.56	4135	317	0.077	0.361	9.39	0.00328	4.39	
0.000352	0.00067	0.40	2689	4.15	2765	158	0.057	0.434	6.36	0.00214	3.19	
0.000352	0.00085	0.39	1389	4.02	3391	188	0.055	0.293	4.80	0.00214	2.52	
0.000352	0.00094	0.45	1389	4.60	4307	273	0.063	0.284	6.29	0.00340	3.62	
0.000352	0.00093	0.61	1389	6.29	5804	503	0.087	0.204	7.63	0.00345	3.73	
0.000352	0.00093	0.65	1389	6.68	6174	567	0.092	0.193	7.99	0.00342	3.68	
0.000352	0.00093	0.65	1389	6.68	6174	567	0.092	0.193	7.99	0.00361	3.89	
0.000352	0.00073	0.90	4636	9.27	6721	858	0.128	0.364	22.20	0.00455	6.25	
0.000352	0.00079	0.74	3210	7.60	6004	628	0.105	0.335	15.47	0.00415	5.23	
0.000352	0.00074	0.35	1844	3.58	2632	130	0.049	0.381	4.65	0.00181	2.45	
0.000352	0.00067	1.65	3973	16.94	11248	2623	0.233	0.156	24.98	0.00426	6.39	
0.000352	0.00073	0.79	3900	8.12	5873	657	0.112	0.349	16.95	0.00416	5.73	
0.000560	0.00140	2.00	1380	8.13	11363	1271	0.112	0.238	18.40	0.00851	6.06	

Table A.1: Continued

Post SH Surface Data													
d_j (m)	d (m)	Q (mL/s)	f (Hz)	V (m/s)	Re	We	Ca	St	$Re^{0.7}(CaSt)$		d_B (m)	d_B/d	d_B/d_j
0.000560	0.00122	2.00	2100	8.13	9879	1105	0.112	0.315	22.08		0.00768	6.29	
0.000560	0.00107	2.00	3100	8.13	8676	970	0.112	0.409	26.14		0.00696	6.50	
0.000560	0.00107	2.00	3100	8.13	8676	970	0.112	0.409	26.14		0.00735	6.86	
0.000560	0.00149	1.50	860	6.09	9065	760	0.084	0.211	10.42		0.00674	4.51	
0.000560	0.00132	1.50	1240	6.09	8024	673	0.084	0.269	12.20		0.00652	4.93	
0.000560	0.00117	1.50	1800	6.09	7087	594	0.084	0.345	14.34		0.00570	4.88	
0.000560	0.00108	1.50	2300	6.09	6531	548	0.084	0.406	15.95		0.00638	5.93	
0.000560	0.00144	1.00	640	4.06	5826	326	0.056	0.227	5.48		0.00367	2.55	
0.000560	0.00129	1.00	900	4.06	5200	291	0.056	0.285	6.36		0.00461	3.59	
0.000560	0.00114	1.00	1300	4.06	4600	257	0.056	0.364	7.45		0.00419	3.68	
0.000560	0.00106	1.00	1600	4.06	4292	240	0.056	0.418	8.16		0.00404	3.81	

.

.

Table A.2: Data for droplet train impingement experiments performed on a rib SH surface used in Chapter 4.

Rib SH Surface Data										Longitudinal		Transverse	
d_j (m)	d (m)	Q (mL/s)	f (Hz)	V (m/s)	Re	We	Ca	St	$Re^{0.7}(CaSt)$	d_B (m)	d_B/d	d_B (m)	d_B/d
0.000560	0.00134	2.1	1670	8.53	11379	1336	0.117	0.262	21.26	0.00671	5.01	0.00816	6.09
0.000560	0.00108	2.1	3150	8.53	9210	1082	0.117	0.400	28.00	0.00579	5.34	0.00733	6.77
0.000560	0.00104	2.1	3568	8.53	8835	1038	0.117	0.435	29.55	0.00579	5.57	0.00761	7.32
0.000560	0.00110	2.5	3573	10.16	11142	1558	0.140	0.387	36.87	0.00660	5.99	0.00857	7.78
0.000560	0.00140	3.3	2320	13.41	18632	3439	0.185	0.241	43.47	0.00928	6.65	0.01185	8.49
0.000560	0.00137	3.3	2430	13.41	18346	3386	0.185	0.249	44.35	0.00914	6.65	0.01190	8.66
0.000560	0.00114	3.3	4230	13.41	15251	2815	0.185	0.360	56.39	0.00879	7.70	0.01101	9.64
0.000560	0.00120	1.87	2070	7.60	9075	949	0.105	0.327	20.15	0.00678	5.65	0.00818	6.82
0.000560	0.00112	1.87	2510	7.60	8511	890	0.105	0.372	21.90	0.00554	4.92	0.00727	6.47
0.000560	0.00110	1.87	2680	7.60	8327	871	0.105	0.388	22.54	0.00512	4.66	0.00694	6.31
0.000560	0.00111	1.5	2100	6.09	6732	565	0.084	0.382	15.33	0.00616	5.56	0.00659	5.94
0.000560	0.00105	1.5	2500	6.09	6352	533	0.084	0.429	16.54	0.00550	5.25	0.00703	6.72
0.000560	0.00104	1.5	2579	6.09	6286	527	0.084	0.438	16.76	0.00524	5.06	0.00644	6.21
0.000560	0.00087	1.5	4370	6.09	5273	442	0.084	0.623	21.07	0.00500	5.75	0.00587	6.76
0.000560	0.00171	2.01	770	8.17	13894	1562	0.112	0.161	14.38	0.00791	4.63	0.01079	6.32
0.000560	0.00123	2.01	2040	8.17	10041	1129	0.112	0.308	21.94	0.00664	5.38	0.00764	6.19
0.000560	0.00108	2.01	3030	8.17	8801	989	0.112	0.402	26.04	0.00596	5.51	0.00758	7.01
0.000560	0.00109	2.82	4200	11.46	12397	1955	0.158	0.398	46.07	0.00759	6.99	0.00913	8.41
0.000560	0.00107	2.82	4400	11.46	12206	1925	0.158	0.411	47.01	0.00784	7.33	0.00902	8.43
0.000560	0.00106	2.82	4500	11.46	12115	1911	0.158	0.417	47.47	0.00815	7.67	0.00961	9.05
0.000560	0.00104	2.82	4750	11.46	11899	1877	0.158	0.432	48.59	0.00764	7.33	0.00930	8.92
0.000560	0.00103	2.82	5000	11.46	11697	1845	0.158	0.447	49.68	0.00730	7.12	0.00834	8.14
0.000560	0.00117	1.6	1910	6.50	7572	678	0.089	0.344	15.97	0.00520	4.45	0.00688	5.88
0.000560	0.00115	1.6	2020	6.50	7432	665	0.089	0.357	16.36	0.00555	4.84	0.00722	6.29
0.000560	0.00112	1.6	2200	6.50	7224	646	0.089	0.378	16.98	0.00599	5.37	0.00657	5.89
0.000560	0.00110	1.46	2100	5.93	6493	530	0.082	0.389	14.82	0.00556	5.06	0.00658	5.98
0.000560	0.00143	2.32	1500	9.43	13470	1748	0.130	0.228	23.03	0.00848	5.91	0.01081	7.54
0.000560	0.00105	2.32	3850	9.43	9838	1276	0.130	0.428	34.65	0.00681	6.50	0.00925	8.83
0.000560	0.00120	1.16	1270	4.71	5650	367	0.065	0.324	8.90	0.00451	3.74	0.00524	4.35
0.000560	0.00113	1.16	1530	4.71	5310	345	0.065	0.367	9.65	0.00411	3.63	0.00540	4.77
0.000560	0.00107	1.16	1830	4.71	5003	325	0.065	0.414	10.43	0.00451	4.23	0.00528	4.95
0.000560	0.00079	1.16	4420	4.71	3729	242	0.065	0.745	15.29	0.00466	5.87	0.00507	6.38
0.000560	0.00116	1.23	1500	5.00	5780	398	0.069	0.349	10.31	0.00431	3.71	0.00547	4.71
0.000560	0.00110	1.23	1750	5.00	5490	378	0.069	0.386	11.02	0.00496	4.50	0.00586	5.32
0.000560	0.00106	1.23	1950	5.00	5296	364	0.069	0.415	11.55	0.00471	4.42	0.00517	4.86
0.000560	0.00125	1.27	1250	5.16	6410	455	0.071	0.302	9.92	0.00471	3.78	0.00610	4.89
0.000560	0.00114	1.27	1650	5.16	5843	415	0.071	0.364	11.19	0.00480	4.22	0.00608	5.35
0.000560	0.00107	1.27	2000	5.16	5480	389	0.071	0.413	12.16	0.00491	4.60	0.00591	5.55
0.000560	0.00082	1.27	4320	5.16	4239	301	0.071	0.691	16.98	0.00512	6.21	0.00598	7.24
0.000560	0.00132	1.33	1100	5.40	7113	529	0.074	0.269	9.95	0.00426	3.22	0.00646	4.89
0.000560	0.00114	1.33	1700	5.40	6153	458	0.074	0.360	12.02	0.00380	3.32	0.00629	5.50
0.000560	0.00109	1.33	1940	5.40	5888	438	0.074	0.393	12.72	0.00453	4.14	0.00643	5.87
0.000560	0.00086	1.33	3970	5.40	4637	345	0.074	0.633	17.35	0.00532	6.17	0.00587	6.81
0.000560	0.00145	0.76	480	3.09	4447	189	0.043	0.225	3.42	0.00290	2.00	0.00292	2.02
0.000560	0.00148	0.9	530	3.66	5391	271	0.050	0.215	4.42	0.00345	2.33	0.00368	2.49
0.000560	0.00120	0.9	1000	3.66	4362	220	0.050	0.328	5.82	0.00300	2.50	0.00328	2.74
0.000560	0.00124	0.97	970	3.94	4870	264	0.054	0.305	6.32	0.00366	2.95	0.00378	3.05

Table A.2: Continued

Rib SH Surface Data													
d_j (m)	d (m)	Q (mL/s)	f (Hz)	V (m/s)	Re	We	Ca	St	$Re^{0.7}(CaSt)$		Longitudinal		Transverse	
											d_B (m)	d_B/d	d_B (m)	d_B/d
0.000560	0.00108	0.97	1470	3.94	4240	230	0.054	0.403	7.56		0.00374	3.46	0.00368	3.40
0.000560	0.00139	2.36	1690	9.59	13243	1748	0.132	0.244	24.78		0.00726	5.23	0.00894	6.45
0.000560	0.00107	2.36	3690	9.59	10208	1347	0.132	0.411	34.76		0.00760	7.11	0.00877	8.21
0.000560	0.00131	2.7	2320	10.97	14258	2153	0.151	0.276	33.71		0.00839	6.43	0.00931	7.13
0.000560	0.00127	2.7	2510	10.97	13889	2097	0.151	0.291	34.88		0.00885	6.96	0.01045	8.22
0.000560	0.00108	2.7	4050	10.97	11841	1788	0.151	0.400	42.92		0.00756	6.98	0.00986	9.10
0.000560	0.00106	2.7	4300	10.97	11607	1753	0.151	0.416	44.05		0.00823	7.75	0.00973	9.16
0.000560	0.00101	2.7	4980	10.97	11053	1669	0.151	0.459	46.94		0.00771	7.62	0.00966	9.55
0.000560	0.00134	2.46	1950	9.99	13345	1836	0.138	0.262	27.79		0.00929	6.93	0.01052	7.85
0.000560	0.00111	2.46	3400	9.99	11087	1525	0.138	0.379	35.36		0.00839	7.53	0.00964	8.65
0.000560	0.00106	2.46	3900	9.99	10592	1457	0.138	0.415	37.52		0.00721	6.78	0.00917	8.62
0.000560	0.00101	2.46	4500	9.99	10098	1389	0.138	0.457	39.93		0.00706	6.96	0.00883	8.70
0.000560	0.00100	2.46	4700	9.99	9953	1369	0.138	0.470	40.68		0.00751	7.52	0.00856	8.57
0.000560	0.00141	2.3	1560	9.34	13142	1690	0.129	0.236	23.17		0.00719	5.09	0.00838	5.94
0.000560	0.00116	2.3	2840	9.34	10763	1384	0.129	0.352	30.04		0.00737	6.37	0.00893	7.72
0.000560	0.00112	2.3	3130	9.34	10420	1340	0.129	0.375	31.33		0.00640	5.72	0.00808	7.22
0.000560	0.00105	2.3	3830	9.34	9742	1253	0.129	0.429	34.19		0.00674	6.44	0.00888	8.48

APPENDIX B. UNCERTAINTY ANALYSIS

The sections of this appendix present the uncertainty analysis for the Reynolds number (Re), Weber number (We), Capillary number (Ca), and Strouhal number (St).

B.1 Reynolds Number

The droplet train experiments utilized the Reynolds number defined as $Re = Vd/\nu$. Through a propagation of uncertainty approach, the uncertainty of Re (χ_{Re}) is determined by:

$$\frac{\chi_{Re}}{Re} = \left[\left(\frac{\chi_V}{V}\right)^2 + \left(\frac{\chi_d}{d}\right)^2 + \left(\frac{\chi_\nu}{\nu}\right)^2\right]^{1/2} \tag{B.1}$$

The uncertainty in ν was due to changes in temperature, with a maximum of 1.3%. The velocity (V) and droplet diameter (d) were not measured directly, but rather in terms of the volume of fluid expelled from the nozzle ($\forall$) over the time required to do so (t). The maximum uncertainty for each was 2.2% and 0.3% respectively. A propagation of uncertainty was used to obtain the following:

$$\frac{\chi_V}{V} = \left[\left(\frac{\chi_\forall}{\forall}\right)^2 + \left(\frac{\chi_t}{t}\right)^2\right]^{1/2} \tag{B.2}$$

$$\frac{\chi_d}{d} = \left[\left(\frac{\chi_\forall}{3\forall}\right)^2 + \left(\frac{\chi_t}{3t}\right)^2\right]^{1/2} \tag{B.3}$$

These uncertainties each had a maximum of 2.5% and 0.7% respectively. The resulting maximum uncertainty in Re was 5%.

B.2 Weber Number

The Weber number ($We = \rho V^2 d/\sigma$) was used in both droplet impingement on liquid coated surfaces and droplet train impingement experiments. The uncertainty in density (ρ) and surface

tension (σ) were neglected. Using propagation of uncertainty gives:

$$\frac{\chi_{We}}{We} = \left[\left(\frac{2\chi_V}{V} \right)^2 + \left(\frac{\chi_d}{d} \right)^2 \right]^{1/2} \tag{B.4}$$

For droplet impingement on liquid coated surfaces, the uncertainty in V and d were 1.4% and 2.4% respectively, the resulting uncertainty in *We* remained below 3%. For the droplet train experiments, V and d, and their respective uncertainties, were calculated as described for *Re* uncertainty, resulting in a maximum uncertainty in *We* of 5%.

B.3 Capillary Number and Strouhal Number

Applying propagation of uncertainty to the Capillary number ($Ca = V\mu/\sigma$) and the Strouhal number ($St = Vd/f$), used in droplet train experiments results in the following equations respectively:

$$\frac{\chi_{Ca}}{Ca} = \left[\left(\frac{\chi_V}{V} \right)^2 + \left(\frac{\chi_\mu}{\mu} \right)^2 \right]^{1/2} \tag{B.5}$$

$$\frac{\chi_{We}}{We} = \left[\left(\frac{\chi_V}{V} \right)^2 + \left(\frac{\chi_d}{d} \right)^2 \right]^{1/2} \tag{B.6}$$

In *Ca*, the uncertainty in σ has been neglected as done previously and the uncertainty in dynamic viscosity (μ) was due to temperature fluctuations, as ν in *Re* was, with a maximum of 1.3%. The frequency (f) uncertainty has also been neglected, being less than 0.01%. The uncertainties in V and d are again the same as for *Re* and *We* uncertainties. The resulting uncertainties for *Ca* and *St* were below 6% and 1.7% respectively.